

Transcriptional Profiling of Primate Central Nucleus of the Amygdala Neurons to Understand the Molecular Underpinnings of Early-Life Anxious Temperament

Rothem Kovner, Tade Souaiaia, Andrew S. Fox, Delores A. French, Cooper E. Goss, Patrick H. Roseboom, Jonathan A. Oler, Marissa K. Riedel, Eva M. Fekete, Julie L. Fudge, James A. Knowles, and Ned H. Kalin

ABSTRACT

BACKGROUND: Children exhibiting extreme anxious temperament (AT) are at an increased risk for developing anxiety and depression. Our previous mechanistic and neuroimaging work in young rhesus monkeys linked the central nucleus of the amygdala to AT and its underlying neural circuit.

METHODS: Here, we used laser capture microscopy and RNA sequencing in 47 young rhesus monkeys to investigate AT's molecular underpinnings by focusing on neurons from the lateral division of the central nucleus of the amygdala (CeL). RNA sequencing identified numerous AT-related CeL transcripts, and we used immunofluorescence ($n = 3$) and tract-tracing ($n = 2$) methods in a different sample of monkeys to examine the expression, distribution, and projection pattern of neurons expressing one of these transcripts.

RESULTS: We found 555 AT-related transcripts, 14 of which were confirmed with high statistical confidence (false discovery rate $< .10$), including protein kinase C delta (PKC δ), a CeL microcircuit cell marker implicated in rodent threat processing. We characterized PKC δ neurons in the rhesus CeL, compared its distribution with that of the mouse, and demonstrated that a subset of these neurons project to the laterodorsal bed nucleus of the stria terminalis.

CONCLUSIONS: These findings demonstrate that CeL PKC δ is associated with primate anxiety, provides evidence of a CeL to laterodorsal bed nucleus of the stria terminalis circuit that may be relevant to understanding human anxiety, and points to specific molecules within this circuit that could serve as potential treatment targets for anxiety disorders.

Keywords: Anxiety, Bed nucleus of the stria terminalis, Central nucleus of the amygdala, Fear, Microcircuitry, Protein kinase C delta (PKC δ), Retrograde tracing, Somatostatin, Stress

<https://doi.org/10.1016/j.biopsych.2020.05.009>

Depending on its intensity and context in which it is expressed, anxiety can be adaptive or maladaptive. Across a population, anxiety is characterized by individual differences and when extreme is disabling. Research has identified heritable and nonheritable factors underlying the development of anxiety disorders (1–4), and during childhood these can manifest as the trait-like disposition anxious temperament (AT). Like anxiety, AT is dimensional and is characterized by individual differences in inhibitory responses to novel and social situations (5–8) as well as threat-related pituitary-adrenal activation (5,9). Because AT reflects a combination of behavioral and physiological responses to stress, this construct reflects the interplay among emotions, behavior, and physiology that is emblematic of anxiety responses. When extreme and stable over time, childhood AT increases the risk for the development of anxiety

disorders, depression, and comorbid substance use disorder later in life (6,7,10–12).

To understand the mechanisms underlying AT, we developed a young rhesus monkey model of individual differences in the expression of dispositional anxiety that is analogous to the phenotype exhibited by at-risk children (13,14). Rhesus monkeys are ideally suited for studies of human psychopathology owing to their recent evolutionary divergence from humans, which is reflected in similarities in brain structure and in their emotional and physiological responding (14). Our approach is to understand individual differences in the AT phenotype in relation to individual differences in its underlying neural and molecular substrates (4,13,15). Using a large multigenerational pedigree, we demonstrated that AT is ~30% heritable, consistent with previous human studies (4,16).

SEE COMMENTARY ON PAGE e35

Numerous studies point to the importance of the extended amygdala in mediating adaptive responses to threat as well as in stress-related psychopathology (13,17,18). Components of the extended amygdala include the central nucleus of the amygdala (Ce) and the bed nucleus of the stria terminalis (BST) (19). The Ce, primarily composed of GABAergic (gamma-aminobutyric acidergic) neurons, coordinates information flow out of the amygdala (20–24). The Ce sends strong projections to the BST, a region also involved in threat responding (25–27). We previously demonstrated that individual differences in Ce and BST metabolism relate to trait-like individual differences in AT (5), that brain metabolism in these regions is heritable, and that BST metabolism, but not Ce metabolism, is coheritable with AT (4). We also demonstrated that neurotoxic lesions of the Ce reduce AT, directly implicating the Ce as a core mechanistic component of the AT circuit (4,28,29).

It is important to emphasize that the Ce is not uniform and can be divided into at least 2 subnuclei, namely the lateral Ce (CeL) and medial Ce (CeM) (30,31). The CeM coordinates the output of the amygdala via its projections to multiple downstream effector sites (24). The CeL modulates the CeM, helping to orchestrate the different behavioral and physiological responses mediated by the CeM's targets (21,32). The entire Ce projects to the BST to further coordinate threat-related responding, where the CeL's projections are largely restricted to the laterodorsal BST (BSTLd) (25,33–35). In addition to other basal forebrain areas, the CeL, CeM, and BSTLd have been conceptualized as the central extended amygdala (19). Rodent studies have traced microcircuits within the extended amygdala that are composed of GABAergic neuronal subtypes acting to mediate anxiety and fear responses (23,32–35). However, these microcircuits have not yet been characterized in primates.

In this study, we characterized individual differences in gene expression in laser microdissected primate CeL neurons in relation to AT and its components by performing RNA sequencing (RNA-Seq). We focused on CeL neurons because of their mechanistic role in mediating primate AT and because of rodent data demonstrating the CeL's role in integrating information and acting as an interface between the basolateral amygdala and the CeM/BSTLd (23,26,36,37). Rodent studies have also highlighted subpopulations of GABAergic CeL neurons, such as those expressing protein kinase C delta (gene: *Prkcd*, *PRKCD*; protein: PKC δ) or somatostatin (gene: *Sst*, *SST*; protein: SST), that have critical roles in modulating fear- and anxiety-related extended amygdala function (20,32,38,39). Here, in addition to our discovery-based approach, we more specifically focused on genes known to distinguish CeL neuronal subtypes. Because the RNA-Seq data revealed relations between *PRKCD* expression and AT, as an initial step to understanding extended amygdala microcircuitry in the primate, we characterized the distribution and projection pattern of PKC δ neurons within the extended amygdala. This approach informs the translational value of rodent anxiety models to primates, and because of the relevance of the rhesus AT model to humans, the findings have the potential to uncover novel molecular targets for the treatment of anxiety disorders and other stress-related psychopathology.

METHODS AND MATERIALS

Complete methods are provided in [Supplement 1](#).

AT Phenotyping

AT is a composite score reflecting threat-related behavioral and cortisol changes elicited by exposure to the no-eye-contact condition of the human intruder paradigm (5). Freezing duration and coo vocalization reductions, along with plasma cortisol levels, were used to compute each individual's AT ([Supplement 1](#)).

Animals

A total of 47 monkeys (*Macaca mulatta*; average age = 2.27 years, SD = 0.46; 24 male and 23 female) were used for RNA-Seq. To understand the AT levels in these 47 animals in relation to a larger population from which they came, we performed an analysis with data from animals that were phenotyped in our laboratory over the last 12 years ($n = 721$, average age = 1.9 years, SD = 0.74; 386 male and 335 female) ([Figure S1B](#) in [Supplement 1](#)). C57BL/6J and KO;B6;129X1-*Prkcd*^{tm1Ms}/J mice (Jackson Laboratory, Bar Harbor, ME) were group housed for at least 7 days before experimentation (12-hour light/dark cycle; ad libitum access to food and water). When 21 days old, mice were perfused (40) and tissue was stored for immunohistochemical studies. Animal housing and experimental procedures were conducted in accordance with institutional guidelines and were approved by the Committee on the Ethics of Animal Research of the University of Wisconsin-Madison.

Laser Capture Microdissection

All monkeys were euthanized under deep anesthesia, 4 days after AT phenotyping, with the guidance of veterinary staff using pentobarbital, consistent with the recommendations of the Panel on Euthanasia of the American Veterinary Medical Association. Fresh frozen tissue was collected, cut into slabs, flash frozen in 2-methylbutane, and stored at -80°C as previously described (41). Then, 14- μm sections from the slab containing the amygdala were obtained on a cryostat at -20°C . Sections throughout the CeL's anterior-posterior (A-P) extent were mounted on Leica PEN (polyethylene naphthalate) 2.0- μm membrane laser capture microdissection (LCM) slides (11532918; Leica, Wetzlar, Germany). Adjacent sections were stained with acetylcholinesterase to localize the Ce ([Figure S2B](#) in [Supplement 1](#)). LCM sections were rapidly stained for NeuN (neuronal nuclei) ([Supplement 1](#)). CeL neurons were dissected with a Leica LMD6500 laser capture microscope. For each animal, 500 to 600 neurons were sampled from 6 to 8 slides (every 0.25 mm). After dissection, each LCM slide image was overlaid with its adjacent acetylcholinesterase slide image in Adobe Illustrator CC 2014 to confirm that cells were dissected from the CeL. Tubes containing a minimum of 80% of neurons captured from the CeL were used, and the percentage of CeL neurons in each of these tubes was used to calculate a CeL neuronal accuracy score ([Supplement 1](#)). Within an animal, tubes were pooled for RNA extraction using Qiagen RNeasy Plus Micro kit (74034; Qiagen, Hilden, Germany).

RNA Sequencing

RNA was sequenced at the University of Southern California by JAK. Samples were processed with NuGen RNA-Seq V2 kit

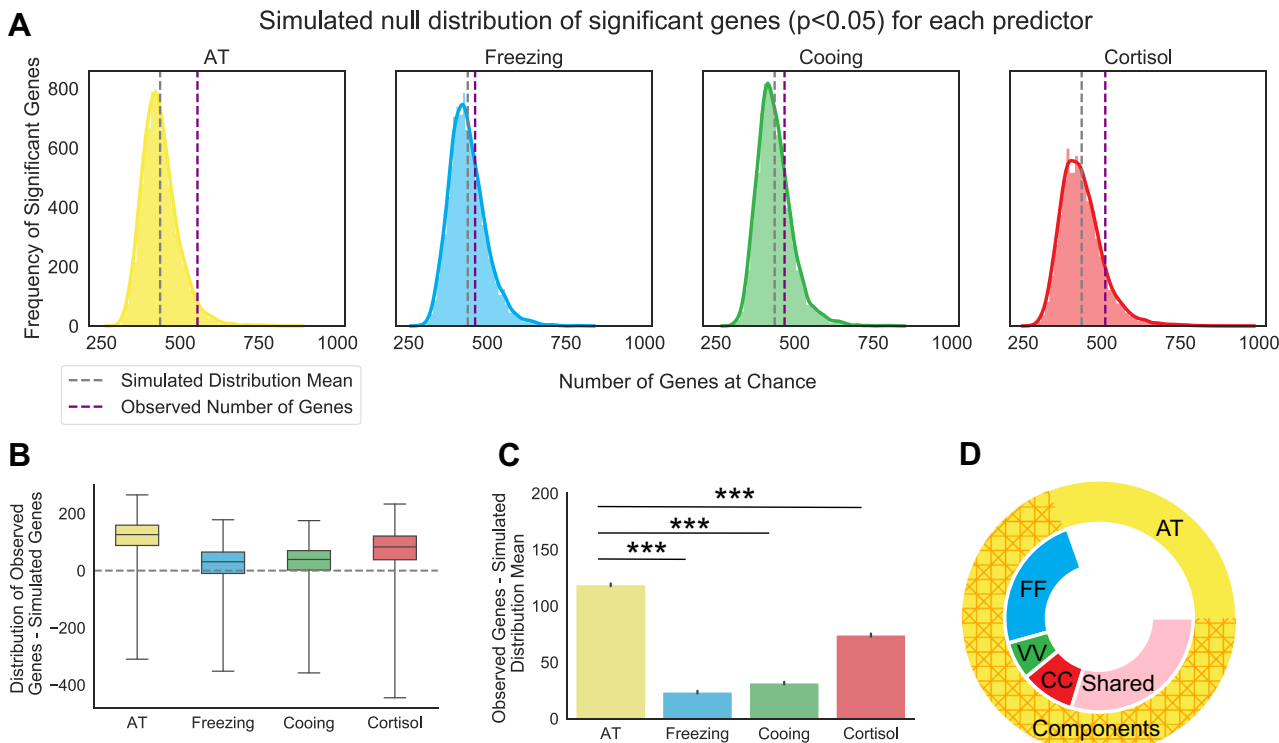


Figure 1. AT predicts a significant number of genes above chance and outperforms each of the AT components. **(A)** Simulated null distribution (as described in Methods and Materials) for each predictor of interest at a nominal p value of $p < .05$. Purple dotted lines indicate the observed number of genes associated with each predictor's real values. Gray dotted lines indicate the mean number of genes of the simulated distribution. The solid colored outline of the distribution represents the density of significant genes as determined by a kernel density estimation. **(B)** Boxplots for each predictor depicting the distribution and mean of the differences between the real observation and each simulated value. Empirical p values were calculated for each predictor (AT: $p = .04$; freezing: $p = .30$; cooing: $p = .24$; cortisol: $p = .12$). **(C)** Barplot demonstrating that AT predicts significantly more genes above the simulated distribution mean than those predicted by each of the AT components alone: freezing ($t = 113.5, p < .001$), cooing ($t = 106.9, p < .001$), or cortisol ($t = 496, p < .001$). Error bars are displayed as SEM. The p values are Sidák corrected for multiple comparisons. AT component values were transformed and residualized as described in Methods and Materials. **(D)** Donut plot depicting the number of overlapping genes between individual AT components and AT. Outside circle represents all 555 AT-related genes ($p < .05$) and is separated into the 383 genes that overlap with AT components (hashed orange) and the 172 genes that are unique to AT (yellow). Inner circle represents genes that are related to AT and is broken up by genes that are also unique to one AT component (FF: freezing in blue; VV: cooing in green; CC: cortisol in red) or that are shared by at least 2 components (Shared in pink). ***significant at $p < .0001$. AT, anxious temperament.

(7102-32; NuGen, San Carlos, CA) for complementary DNA synthesis and with NuGEN Ovation Rapid Library kit (0319 and 0320) for library preparation. The Illumina HiSeq 2500 with regular rapid sequencing prep kit was used (Illumina, San Diego, CA). Reads were single end and targeted to be 100 base pairs in length. A mean of 949710 mapped reads was found across animals. Reads were mapped to MacaM 7.8 (42). Mapping was performed using Sequence Alignment for Gene Expression (<https://github.com/tadesouaiaia/sage>) written in Python 2.7.

RNA-Seq Analysis and Model Evaluation

Genes with 1 read in at least 20% of the animals were used for quantile normalization. Data were log₂ transformed, and fully annotated genes where at least 50% of the samples expressed more than 1 mapped read were used in ordinary least squares (OLS) regression. We built statistical models that assessed the association between gene expression and the predictor of interest. AT, freezing, cooing, and cortisol measured closest to time of death were used as predictors. The statistical model

was built within a framework designed to maximize power to detect predictor-related associations while also reducing false positives discovered with permutation analysis. We focused on models that described the largest fraction of the variance (R^2) across the transcriptome without overfitting.

Variables were tested in relation to transcriptome-wide gene expression to identify potential covariates and were tested for collinearity (Figure S3A in Supplement 1). Two measures (Ce neuron accuracy and age at necropsy) were selected because they were not multicollinear and had the greatest number of positive genes relative to false positives in a simulation (Supplement 1 and Table S1 in Supplement 2). Using Ce neuron accuracy and age at necropsy as covariates separately and together, we tested models to establish whether they could detect predictor-related gene expression relationships above chance. Sex was not included because it did not perform better than a pseudovariable and did not improve upon the variance accounted for by a model without sex (Table S2 in Supplement 2). We chose the models using both neuron accuracy and age at necropsy because they had the

Table 1. Verified Gene Hits That Pass Multiple Comparison Correction Across Two Different Statistical Methods

Gene	Functions of Interest ^a	AT Relation ^b
chr18: SS18	Nuclear receptor transcription coactivator activity (GO:0030374) Positive regulation of transcription, DNA templated (GO:0045893)	—
chr02a: DNMT3A	DNA binding (GO:0003677) Chromatin binding (GO:0003682)	+
chr05: ZNF300	Sequence-specific DNA binding (GO:0043565)	—
chr03: PRKCD	Intracellular signal transduction (GO:0035556) Protein kinase C activity (GO:0004697)	+
chr06: SH3BGRL2	SH3 domain binding (GO:0017124)	+
chr15: BCR	Protein binding (GO:0005515)	+
chr16: FBXL16	Ubiquitin–protein transferase activity (GO:0004842)	+
chr02a: AFTPH	Clathrin binding (GO:0030276) Intracellular transport (GO:0046907)	+
chr17: DYNLL2	Dynein light intermediate chain binding (GO:0051959)	—
chr10: SLC18A2	Monoamine transmembrane transporter activity (GO:0008504)	+
chr06: KIAA1009	Protein binding (GO:0005515)	—
chr01: MGST3	Glutathione transferase activity (GO:0004364)	+
chr09: KIAA1045	Regulation of synaptic transmission, GABAergic (GO:0032228)	+
chr16: C16orf87	Protein binding (GO:0005515)	+

AT, anxious temperament; GABAergic, gamma-aminobutyric acidergic; GO, Gene Ontology.

^aFunctions of interest were chosen based on ontologies that contain these genes.

^bAT relation indicates the direction of the gene expression correlation with AT.

lowest Bayesian information criterion, accounted for the greatest percentage of the variance, and had the fewest false positives in a simulated model. In the models using AT, freezing, cooing, and cortisol as predictors, the predictor was shuffled and correlated with gene expression. Chance distributions were constructed with 10,000 simulations for each predictor (Figure 1A) to assess the signal strength relative to noise. The final model was used to determine differentially expressed genes associated with each predictor. OLS regression and permutation testing (Supplement 1) were performed in Python 2.7. Another differential gene expression analysis was performed using DESeq2 (43). Gene ontologies were investigated using Panther (44).

RESULTS

AT as a Predictor of the CeL Neuronal Transcriptome Compared With Its Individual Components

LCM was combined with RNA-Seq to identify CeL neuronal gene expression (Figures S2A and S3B, C in Supplement 1) associated with individual differences in AT and its components (Figure 1A). Because our previous work demonstrated that AT accounts for greater variance in CeL metabolism than its components (45), we explored the hypothesis that AT would better predict gene expression than each of its components. After demonstrating that the AT scores of the 47 animals used here were representative of a larger population ($n = 721$) (Figure S1B and Supplemental Results in Supplement 1), multiple regression was used to investigate the relation between gene expression and each predictor (AT, freezing, cooing, and cortisol). We performed a permutation analysis where 10,000 shuffles were performed for each predictor and correlated with transcript expression to construct simulated

null distributions of the number of genes associated with each predictor at chance (Figure 1A). Results demonstrated that AT performed significantly better than chance (empirical $p = .04$) (Figure 1B), whereas AT's individual components did not. Furthermore, the number of genes that were above chance predicted by AT was significantly greater than the number predicted by AT's components (Figure 1C). In total, 555 genes were significantly associated with AT, 383 genes were significantly associated with at least one of AT's components, and 172 genes were significantly and selectively correlated with AT (Figure 1D, Supplemental Results, and Figure S5 in Supplement 1). A similar pattern was observed after performing a weighted gene coexpression network analysis (Supplemental Results and Figure S6 in Supplement 1).

Specific CeL Neuronal Transcripts Associated With AT

Two different approaches were used to identify AT-associated genes. Using DESeq2 (43), which uses a negative binomial model, we identified 716 AT-related genes ($p < .05$) (Table S2 in Supplement 2), constituting 11% of the total genes tested, with 42 genes passing multiple comparison correction (false discovery rate [FDR] $< .10$). In addition, we also used an OLS approach with log-transformed data, which identified 555 AT-related transcripts, comprising 6% of the total genes tested ($p < .05$) (Table S2 in Supplement 2). To account for multiple testing, we performed a nonparametric permutation test on the correlation between AT and gene expression, identifying 20 genes ($FDR < .10$) (Supplement 1). The conjunction of the FDR-corrected genes between the DESeq2 and OLS analyses yielded 14 genes (Table 1 and Table S2 in Supplement 2). Gene Ontology (GO) enrichment analyses on the genes identified with each approach (Figure 2A) demonstrated several biological processes (Table S3 in Supplement 2) in common,

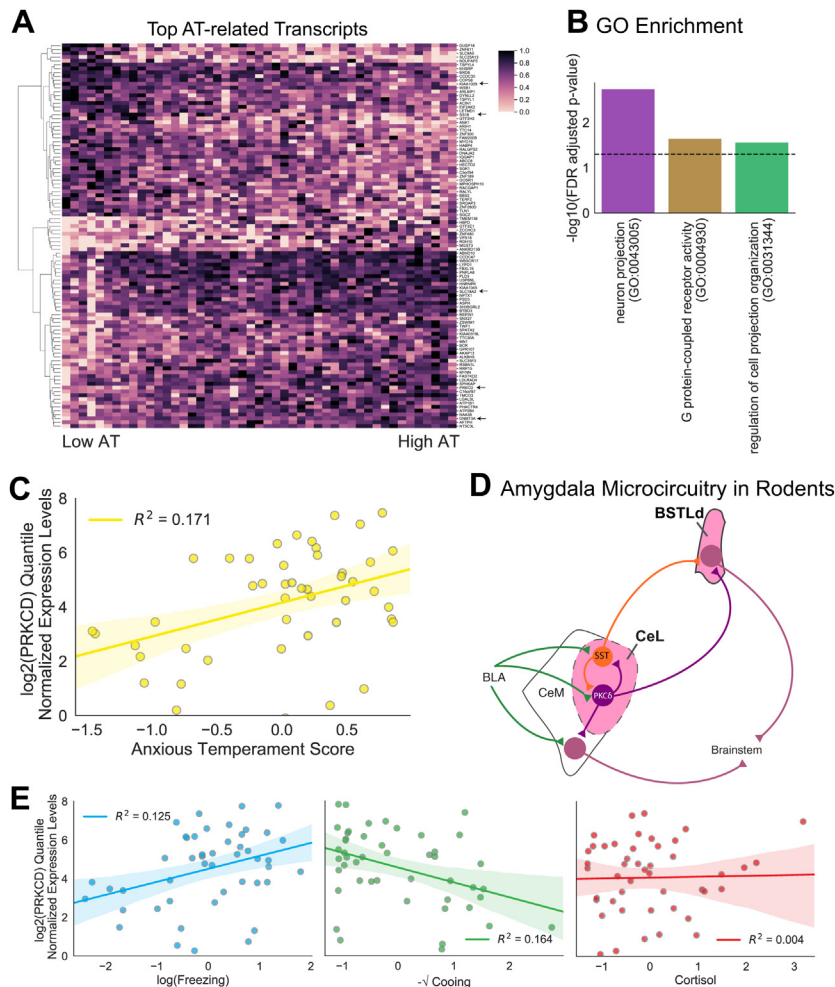


Figure 2. RNA-Seq of LCM CeL neurons revealed AT-related genes. **(A)** Heatmap displaying the top 100 AT-related genes from the intersection of the OLS and DESeq2 analyses ($p < .05$). Gene expression data are presented as quantile normalized min-max scaled values. Arrows point to genes that are discussed in the text. **(B)** Subset of GO enrichment groups for cellular component (purple), molecular function (yellow), and biological process (green) that overlap between approaches. The FDR-corrected p value is depicted by the black dashed line. FDR values reflect those from the OLS ontology. All statistics can be found in Table S2 in Supplement 2. **(C)** Correlation between *PRKCD* mRNA expression levels and AT ($R^2 = .171$). Shaded areas represent the SEM. **(D)** Simplified diagram of the microcircuit within the rodent amygdala and extended amygdala. PKC δ -expressing neurons are labeled in purple. SST-expressing neurons are labeled in orange. Previous work demonstrated that both SST- and PKC δ -expressing neurons receive information from the BLA and contribute to an inhibitory microcircuit within the CeL (32,38,39). Both cell types also project to the BSTLd, while PKC δ -expressing neurons, but not SST-expressing neurons, project to the CeM (32,38,39). **(E)** Correlations between *PRKCD* mRNA expression levels and the individual components of AT (freezing: $R^2 = .125$; cooing: $R^2 = .164$; cortisol: $R^2 = .004$; OLS regression). Freezing, cooing, and cortisol values were standardized, transformed, and residualized as described in Methods and Materials. *PRKCD* mRNA expression levels are presented as quantile normalized \log_2 transformed values residualized for age at ToD and CeL neuron accuracy. AT, anxious temperament; BLA, basolateral amygdala complex; BSTLd, laterodorsal bed nucleus of the stria terminalis; CeL, lateral division of the central nucleus of the amygdala; CeM, medial division of the central nucleus of the amygdala; FDR, false discovery rate; GO, Gene Ontology; LCM, laser capture microdissection; mRNA, messenger RNA; PKC δ , protein kinase C delta; OLS, ordinary least squares; RNA-Seq, RNA sequencing; SST, somatostatin; ToD, time of death.

including neuron projection (GO:0043005), cell projection regulation (GO:0031344), and G-protein receptor activity (GO:0031344) (Figure 2B and Table S3 in Supplement 2).

Among the 14 transcripts that passed FDR correction with both methods, several were related to epigenetic mechanisms such as *SS18* (the SS18 subunit of BAF chromatin remodeling complex) and *DNMT3A* (DNA methyltransferase 3). Also of interest was *KIAA1009* because of its role in primary cilia function in adult cells (46) and its link to schizophrenia (47) and cognitive function (48–50). Another potentially exciting transcript was *SLC18A2* (solute carrier family 18 member A2), a vesicular transport protein critical to monoaminergic neurotransmission (51–54). We also identified *PRKCD* (Figure 2A, C), which is particularly interesting because in rodents it marks a CeL neuron population involved in threat processing and Pavlovian learning (Figure 2D) (32,55,56). CeL *PRKCD* neurons decrease their firing in response to a conditioned stimulus and interact with SST neurons to increase freezing behavior (32). In addition, studies demonstrate that CeL *PRKCD* neurons project to the BST (39), and some of these cells play a role in negative reinforcement learning (55). Moreover, neurotrophic

signaling, which is associated with AT and neuropsychiatric disorders (41,51,57,58), interacts with PKC δ (52). In addition, *PRKCD* messenger RNA (mRNA) expression was also associated with increased freezing and decreased cooing but not with threat-related cortisol (Figure 2E), suggesting that it may be more strongly associated with the behavioral components of AT.

Characterizing PKC δ and SST Neurons in the Monkey CeL

While PKC δ has been extensively studied in the rodent CeL (32,39,53,55,56), little is known about its expression in the monkey. Within the CeL, many neuronal subtypes exist (54,59–61), and mouse studies reveal that SST neurons modulate PKC δ neurons (22,38,62). Because these cell types have not been well characterized in monkeys, we used stereological cell counting to map CeL PKC δ and SST neurons (Figure 3). To further understand the extent to which the mouse studies are translatable to primates, we also performed studies in the mouse CeL (Figure 3B, C). In the monkey CeL, PKC δ neurons accounted for 59% of the estimated total neurons and

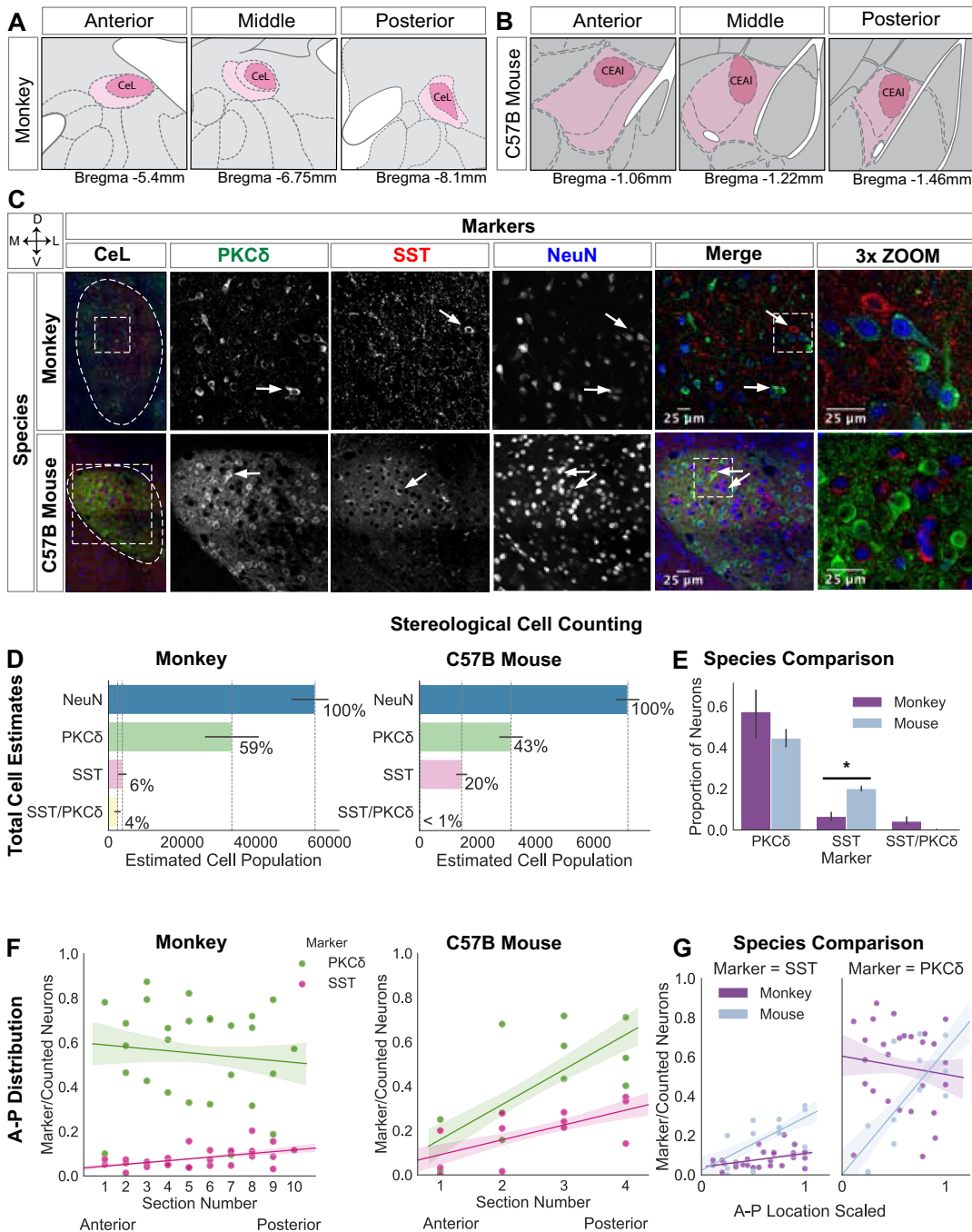


Figure 3. PKC δ -expressing neurons in the monkey CeL compared with the mouse CeL. **(A, B)** CeL atlas slices depicting the A-P extent in the rhesus monkey (**A**) (83) and in the mouse (**B**) (Allen Brain Atlas). **(C)** Representative confocal images of the CeL in both species. White arrows point to PKC δ and SST neurons. Images were adjusted using the Fiji despeckle filter (84) for removing salt and pepper noise. **(D)** Stereological cell estimates for monkey ($n = 3$) and mouse ($n = 3$). **(E)** Species comparison of PKC δ , SST, and PKC δ /SST estimates are presented as a proportion of the total number of neurons (PKC δ : $t = -1.06$, $p = .34$; SST: $t = 3.6$, $p = .02$; t test). Error bars are SEM. **(F)** A-P distribution of PKC δ - and SST-expressing neurons in monkey and mouse (monkey: PKC δ $t = -0.39$, $p = .70$ and SST $t = 2.7$, $p = .012$; mouse: PKC δ $t = 3.1$, $p = .01$ and SST $t = 2.6$, $p = .02$; OLS regression). **(G)** Species comparison of the A-P distribution of each cell type: A-P location \times species interaction for PKC δ ($t = 2.6$, $p = .01$) and A-P location \times species interaction for SST ($t = 2.7$, $p = .01$); OLS regression. To compare A-P distribution between species, A-P location was min-max scaled, with 0 indicating more anterior slices and 1 indicating more posterior slices. A-P, anterior-posterior; CeL, lateral division of the central nucleus of the amygdala; NeuN, neuronal nuclei; OLS, ordinary least squares; PKC δ , protein kinase C delta; SST, somatostatin.

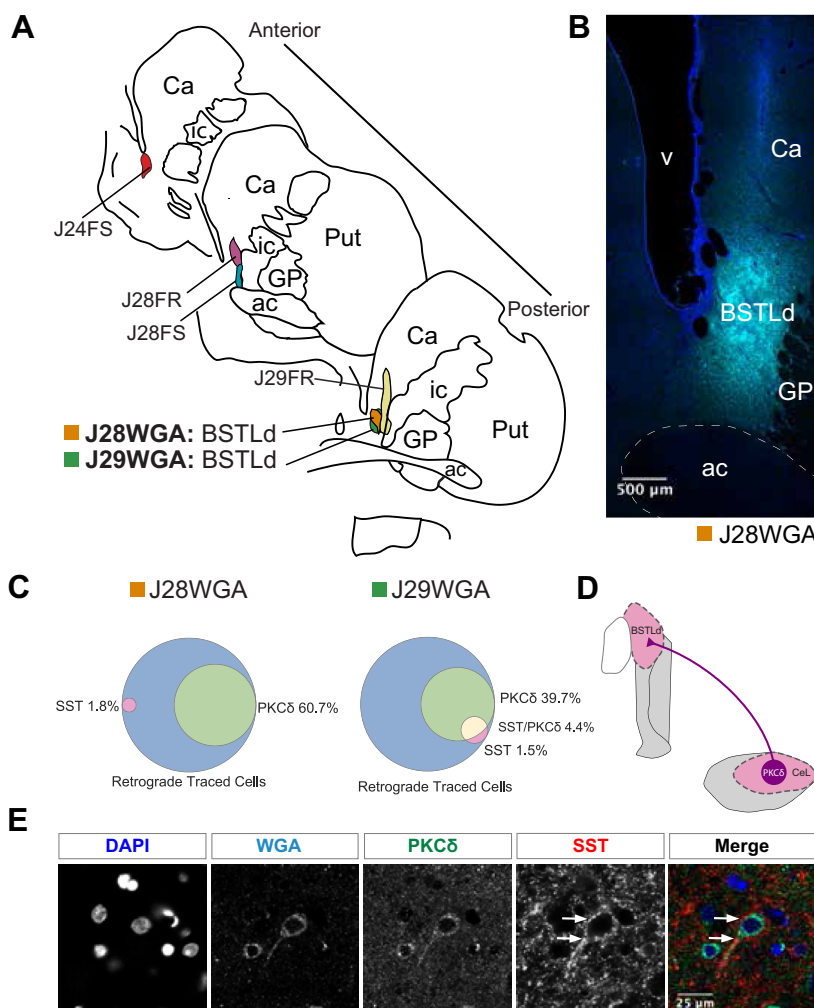


Figure 4. A subset of PKC δ -expressing neurons project to the BSTLd in the monkey. **(A)** Hand-drawn slices depicting the localization of retrograde tracer into different regions of the BST in monkey. Two replicates, J29WGA and J28WGA, are localized to the same part of the BSTLd. **(B)** Representative confocal image of the BSTLd injection site. DAPI staining is in blue. WGA tracer staining is in cyan. **(C)** A Venn diagram for each BSTLd replicate, J29WGA and J28WGA, illustrating the percentage overlap between the WGA tracer and PKC δ , SST, or both. **(D)** Simplified diagram of our results demonstrating that CeL PKC δ -expressing neurons project to the BSTLd in nonhuman primates. **(E)** Representative confocal image of a BSTLd-projecting neuron that expresses PKC δ . This image was adjusted using the Fiji despeckle filter (84) for removing salt and pepper noise. White arrows point to the immense SST innervation received along this neuron's primary dendrite and soma. ac, anterior commissure; BST, bed nucleus of the stria terminalis; BSTLd, laterodorsal bed nucleus of the stria terminalis; Ca, caudate; Cel, lateral division of the central nucleus of the amygdala; GP, globus pallidus; ic, internal capsule; PKC δ , protein kinase C delta; Put, putamen; SST, somatostatin; v, ventricle; WGA, wheat germ agglutinin.

SST neurons accounted for 6% (Figure 3D). In the mouse CeL, PKC δ neurons constituted 43% of the estimated total neurons and SST neurons accounted for 20% (Figure 3D). While the proportions of PKC δ neurons did not significantly differ between species ($t = -1.06, p = .34$) (Figure 3E), the proportion of SST cells was notably decreased in the monkey compared with the mouse ($t = -3.6, p = .02$) (Figure 3E). In monkeys 4% of neurons expressed SST and PKC δ , while in mice this population was nonexistent (Figure 3D).

Previous studies demonstrated that cell types are differentially distributed across the Ce's A-P extent, suggesting A-P functional differences (32,63,64). Consistent with this, PKC δ neurons ($t = 3.1, p = .01$) and SST neurons ($t = 2.6, p = .02$) were significantly more concentrated in the posterior mouse CeL (Figure 3F). In the monkey, SST somata were more concentrated in the posterior CeL ($t = 2.7, p = .012$) (Figure 3F), replicating previous observations (65). However, deviating from the mouse, monkey PKC δ neurons were not differentially distributed across the A-P extent ($t = -0.39, p = .70$). The

interaction between A-P location and species was tested separately for PKC δ and SST neurons and demonstrated significant interactions (PKC δ : $t = 2.6, p = .01$; SST: $t = 2.7, p = .01$) (Figure 3G).

In contrast to the small number of CeL SST neurons, and consistent with previous work, we found dense SST neuropil throughout the monkey CeL (64–67). Numerous SST varicosities were present in close apposition to the primary dendrite and soma of large CeL neurons, a number of which expressed PKC δ (Figure 3C), suggesting that in monkeys SST input may modulate CeL PKC δ neurons. Compared with the limited distribution profile described in the mouse (32), monkey *PRKCD* expression was widely distributed across the brain (Figure S7 in Supplement 1).

A Subset of CeL PKC δ Neurons Project to the BSTLd in the Monkey

In rodents, in addition to constituting an intra-CeL microcircuit, *Prkcd* and *Sst* neurons project to other parts of the extended

Table 2. Number and Percentage of Retrograde Tracer-Labeled Cells Expressing Markers of Interest for Each Case of Retrograde Injection

Case ID	Retrograde Tracer Type	Number of Retrograde-Labeled Cells	Retrograde-Labeled Cells Expressing PKC δ		Retrograde-Labeled Cells Expressing SST		Retrograde-Labeled Cells Expressing PKC δ and SST	
			n	%	n	%	n	%
J24FS	FS	8	1	12.5	1	12.5	0	0
J28FS	FS	23	8	34.8	2	8.7	0	0
J28FR	FR	8	6	75.0	0	0	0	0
J29FR	FR	2	1	50.0	0	0	0	0
J28WGA	WGA	56	34	60.7	2	1.8	0	0
J29WGA	WGA	136	54	39.7	2	1.5	6	4.4

FR, fluororuby; FS, fluorescein; PKC δ , protein kinase C delta; SST, somatostatin; WGA, wheat germ agglutinin.

amygdala (35,39,68). For example, *Prkcd* neurons project to the CeM, and both *Prkcd* and *Sst* neurons project to the BSTLd (Figure 4D) (32,35,39,68), suggesting that these neurons may coordinate CeL and BSTLd in mediating threat-related behaviors. Because of the lack of data in primates and the known species differences in extended amygdala organization (25), we characterized whether CeL PKC δ and SST neurons project to the BSTLd in monkeys. In 6 cases, retrograde tracers were injected into different BST subregions, and in 2 of these cases the injections were centered in the BSTLd (J29WGA and J28WGA) (Figure 4A, B). Tissue was colabeled for the retrograde tracer, DAPI, PKC δ , and SST. Consistent with our previous observations from these monkeys (25), the cases with injections directly into the BSTLd (Figure 4A, B) demonstrated substantially more CeL retrograde-labeled cells (Table 2). In these 2 cases, CeL retrograde-labeled cells expressing PKC δ ranged from 40% to 60% (Figure 4C). In contrast, few retrograde-labeled cells exclusively expressed SST or coexpressed SST and PKC δ (Figure 4C). Adding to our previous observation, SST varicosities also surrounded some CeL to BSTLd-projecting neurons, a subset of which expressed PKC δ (Figure 4D). These data demonstrate that a subset of PKC δ neurons project to the BSTLd, and that SST input likely modulates this projection.

DISCUSSION

Preclinical and clinical research has characterized the neural circuitry underlying fear and anxiety processing. In rodents, molecular studies have been performed to identify potential molecules that modulate the function of these critical neural circuits. Monkey studies are critical for translating these findings to humans, and in this regard the AT model has been extremely helpful. An essential step for understanding mechanisms associated with maladaptive anxiety and in guiding new treatment development is to systematically characterize gene expression alterations in monkeys.

Here, we used a dimensional approach in AT-phenotyped monkeys that follows the presentation of human anxiety. Our previous neuroimaging work supports the dimensionality of the AT construct at a circuit level, and our search for AT-related transcripts is based on this premise. While the subsample used here did not display the highest degree of AT, the range

of AT values within the subsample is representative of the larger population. In these 47 animals, we performed RNA-Seq on neurons captured from the CeL, a region critically involved in gating threat responses (20). Consistent with our previous work (45), we find that AT predicts CeL gene expression better than each of its components alone, but also that individual genes can be component-specific or component-general. This suggests that the variance in CeL gene expression can be better explained by the behavioral and endocrine AT composite than by each AT component alone, but also that specific genes or gene modules may be AT related and still independently associated with specific AT components.

Our ontology analysis revealed overlaps between AT-associated genes and previously identified AT-related molecular pathways (41,58). Here, a number of transcripts reflect genes that are involved in epigenetic mechanisms (*SS18* and *DNMT3A*) (69,70), which is interesting because our earlier work suggested that AT-related Ce metabolism is predominantly affected by nonheritable factors (4). The current findings provide a molecular pathway by which epigenetic mechanisms may influence Ce function, which is particularly relevant to psychiatric disorders that are precipitated by stress (4,71).

We also identified *KIAA1009* and *SLC18A2* as AT related. *KIAA1009* codes for a protein located at the base of primary cilia (46); interestingly, primary cilia alterations are implicated in reduced adult neurogenesis (49), poor novel object learning (48), and schizophrenia (47,72). In addition, *SLC18A2*, which codes for VMAT2, is critical for monoaminergic neurotransmission and has been proposed as a possible drug target for some neuropsychiatric disorders (51–54). Taken together, these data support further investigation of these genes in amygdala function and psychopathology. Previously, we found an association between the truncated isoform of *NTRK3* and AT (58). However, the relatively low amount of RNA acquired with LCM precluded us from confidently examining the relations between AT and isoforms of *NTRK3*.

It is particularly exciting that CeL *PRKCD* mRNA expression was associated with AT given that numerous rodent studies demonstrate that CeL *Prkcd* neurons are part of a microcircuit that modulates freezing behavior (22,32,38,56,73). Our systematic immunohistochemical characterization revealed that 59% of primate CeL neurons express PKC δ . This raises the possibility that the relation between *PRKCD* mRNA and AT

could be accounted for by differences in the number of PKC δ neurons rather than differences in the expression level of PKC δ within the same number of PKC δ neurons. Unfortunately, because the tissue was fresh frozen for RNA-Seq, immunohistochemical staining could not be performed in the tissue from these animals.

Cross-species studies demonstrate that the CeL sends major projections to the BSTLd (23,25,33,35,39). We assessed the extent to which monkey CeL PKC δ neurons project to the BSTLd. Using retrograde tracers introduced into the BSTLd, we found that CeL PKC δ neurons constituted approximately half of the identified CeL to BSTLd-projecting neurons. These data demonstrate that PKC δ neurons originating in the CeL project to the BSTLd. Our previous studies demonstrated that the Ce and BST are part of the neural circuit underlying AT (4), and the current data suggest a plausible pathway by which the CeL interacts with the BSTLd to coordinate AT-relevant responses. It is important to consider that approximately half of the retrograde-labeled neurons did not express PKC δ , suggesting that other CeL neuronal populations could be involved in mediating AT (33,74,75). We note that while *Macaca mulatta* was used in the RNA-Seq experiment, *Macaca fascicularis* was used in the tract-tracing experiments; although the species are highly similar, this is a potential limitation.

Rodent studies point to the importance of CeL PKC δ cells in threat responding but do not address the role of the actual PKC δ protein. While the function of the PKC δ protein in threat processing is unknown, PKC δ is involved in the phospholipase C/PIP₂/diacyl glycerol pathway, a secondary messenger system shared by neurotrophic (76), chemokine, and membrane steroid signaling (77–79). Future studies manipulating CeL PKC δ expression will help discern the potential therapeutic value of targeting PKC δ .

CeL *Prkcd* neurons interact with other neuronal populations, including Sst neurons (22,32,38). While SST mRNA was not associated with AT, because of its potential modulatory role, we also systematically characterized CeL SST neurons. In the monkey, SST neurons constituted a smaller population than in the mouse; however, both species demonstrated dense CeL SST neuropil (54,64,67). We further examined monkey CeL SST varicosities and found that they have close appositions to the somata and primary dendrites of some CeL to BSTLd-projecting neurons, including PKC δ neurons. The origin of the SST innervation in the monkey CeL is unknown. However, SST is expressed in GABAergic neuronal subtypes, and a limited number of GABAergic regions send input to the CeL, including the BST, the sublenticular extended amygdala, and the amygdala intercalated cell masses (23,25,35,80,81). In addition, local CeL SST neurons may also be the source of the dense SST neuropil (22,38,66,82). Future studies that focus on understanding the origins of CeL SST input and the effects of SST release on CeL PKC δ neurons will further our understanding of primate AT-relevant microcircuits.

This transcriptome-wide study in monkey CeL neurons provides a molecular basis for understanding alterations related to the early-life risk of developing psychopathology. This is the first study to characterize gene expression in monkey CeL neurons and to implicate CeL PKC δ neurons as components of a microcircuit relevant to primate anxiety and

AT. To provide a deeper understanding of primate CeL, we systematically characterized PKC δ neurons and found potentially relevant species differences. We demonstrate that a subset of CeL PKC δ neurons project to the BSTLd and may be modulated by SST. These findings present evidence supporting a primate extended amygdala microcircuit relevant to understanding human anxiety and point to specific molecules within this circuit that could serve as potential treatment targets for anxiety disorders.

ACKNOWLEDGMENTS AND DISCLOSURES

This work was supported by funding from the National Institute of Mental Health (Grant Nos. R01MH081884 and R01MH046729 [to NHK], No. R01MH063291 [to JLF], and No. 5T32MH018931 [to RK]) and by grants to the Wisconsin National Primate Center Research Center (Grant Nos. P51-OD011106 and P51-RR000167) and the California National Primate Research Center (Grant No. P51OD011107). Confocal microscopy was performed at the University of Wisconsin–Madison Biochemistry Optical Core, which was established with support from the University of Wisconsin–Madison Department of Biochemistry Endowment.

RK, ASF, JAO, PHR, and NHK conceptualized the study. NHK and ASF oversaw the study. RK, MKR, and EMF collected behavioral data. RK and DAF developed the rapid staining LCM microscopy method and collected the RNA data. DAF performed RNA extractions. JAK and his group performed RNA-Seq. TS aligned the RNA-Seq data. RK and TS analyzed the RNA-Seq data. RK, MKR, and PHR collected tissue, and PHR assessed cortisol. JLF, NHK, and RK conceptualized the stereology study. RK and CEG collected and analyzed the stereology data. JLF performed retrograde tracer surgeries and collected injected tissue. RK performed triple labeling of tracing experiments and microscopic analysis. RK and NHK wrote the manuscript.

We thank the Neuroscience Training Program at the University of Wisconsin–Madison, the personnel of the Harlow Center for Biological Psychology, the HealthEmotions Research Institute, the Waisman Laboratory for Brain Imaging and Behavior, the Wisconsin National Primate Research Center, the Wisconsin Institutes for Medical Research, S. Shelton, and H. Van Valkenberg. We thank L. Kordyban, A. Meier, J. Schnabel, and A. Elmers for help with LCM, M. Kenwood for assistance with collating and analyzing the population behavioral data, and K. Peelman for help with the mouse perfusions.

This article was published as a preprint on bioRxiv: <https://doi.org/10.1101/808279>.

NHK has received honoraria from CME Outfitters, Elsevier, and the Pritzker Consortium; has served on scientific advisory boards for Actify Neurotherapies and Neuronetics; currently serves as an advisor to the Pritzker Neuroscience Consortium and as a consultant to Cocept Therapeutics; has served as coeditor of Psychoneuroendocrinology and currently serves as editor-in-chief of the *American Journal of Psychiatry*; and has patents on promoter sequences for corticotropin-releasing factor CRF2 α and a method of identifying agents that alter the activity of the promoter sequences (Patent Nos. 7,071,323 and 7,531,356), promoter sequences for urocortin II and the use thereof (Patent No. 7,087,385), and promoter sequences for corticotropin-releasing factor binding protein and the use thereof (Patent No. 7,122,650). The other authors report no biomedical financial interests or potential conflicts of interest.

ARTICLE INFORMATION

From the Department of Psychiatry (RK, DAF, CEG, PHR, JAO, MKR, EMF, NHK), Neuroscience Training Program (RK, PHR, NHK), and HealthEmotions Research Institute (RK, DAF, PHR, JAO, MKR, EMF, NHK), University of Wisconsin–Madison, Madison, Wisconsin; Department of Cell Biology (TS, JAK), State University of New York Downstate Medical Center, Brooklyn, New York; Department of Psychiatry (JLF) and Department of Neuroscience/Del Monte Institute for Brain Research (JLF), University of Rochester Medical Center, Rochester, New York; and Department of Psychology (ASF) and

California National Primate Research Center (ASF), University of California, Davis, Davis, California.

Address correspondence to Rothen Kovner, Ph.D., at kovnerrothem@gmail.com or rkovner@wisc.edu, or Ned H. Kalin, M.D., at nkalin@wisc.edu.

Received Dec 9, 2019; revised Apr 22, 2020; accepted May 10, 2020.

Supplementary material cited in this article is available online at <https://doi.org/10.1016/j.biopsych.2020.05.009>.

REFERENCES

1. Stein MB, Jang KL, Livesley WJ (1999): Heritability of anxiety sensitivity: A twin study. *Am J Psychiatry* 156:246–251.
2. Sawyers C, Ollendick T, Brodtman MA, Pine DS, Leibenluft E, Carney DM, et al. (2019): The genetic and environmental structure of fear and anxiety in juvenile twins. *Am J Med Genet B Neuropsychiatr Genet* 180:204–212.
3. Eley TC, Bolton D, O'Connor TG, Perrin S, Smith P, Plomin R (2003): A twin study of anxiety-related behaviours in pre-school children. *J Child Psychol Psychiatry* 44:945–960.
4. Fox AS, Oler JA, Shackman AJ, Shelton SE, Raveendran M, McKay DR, et al. (2015): Intergenerational neural mediators of early-life anxious temperament. *Proc Natl Acad Sci U S A* 112:9118–9122.
5. Fox AS, Shelton SE, Oakes TR, Davidson RJ, Kalin NH (2008): Trait-like brain activity during adolescence predicts anxious temperament in primates. *PLoS One* 3:e2570.
6. Biederman J, Hirshfeld-Becker DR, Rosenbaum JF, Herot C, Friedman D, Snidman N, et al. (2001): Further evidence of association between behavioral inhibition and social anxiety in children. *Am J Psychiatry* 158:1673–1679.
7. Davidson RJ, Rickman M (1999): Behavioral inhibition and the emotional circuitry of the brain: Stability and plasticity during the early childhood years. In: Schmidt LA, Schukin J, editors. *Extreme Fear, Shyness, and Social Phobia: Origins, Biological Mechanisms, and Clinical Outcomes*. New York: Oxford University Press, 67–87.
8. Hirshfeld DR, Rosenbaum JF, Biederman J, Bolduc EA, Faraone SV, Snidman N, et al. (1992): Stable behavioral inhibition and its association with anxiety disorder. *J Am Acad Child Adolesc Psychiatry* 31:103–111.
9. Kagan J, Reznick JS, Snidman N (1987): The physiology and psychology of behavioral inhibition in children. *Child Dev* 58:1459–1473.
10. Essex MJ, Klein MH, Slattery MJ, Goldsmith HH, Kalin NH (2010): Early risk factors and developmental pathways to chronic high inhibition and social anxiety disorder in adolescence. *Am J Psychiatry* 167:40–46.
11. Chronis-Tuscano A, Degnan KA, Pine DS, Perez-Edgar K, Henderson HA, Diaz Y, et al. (2009): Stable early maternal report of behavioral inhibition predicts lifetime social anxiety disorder in adolescence. *J Am Acad Child Adolesc Psychiatry* 48:928–935.
12. Fox NA, Henderson HA, Marshall PJ, Nichols KE, Ghera MM (2005): Behavioral inhibition: Linking biology and behavior within a developmental framework. *Annu Rev Psychol* 56:235–262.
13. Fox AS, Kalin NH (2014): A translational neuroscience approach to understanding the development of social anxiety disorder and its pathophysiology. *Am J Psychiatry* 171:1162–1173.
14. Kalin NH, Shelton SE (2003): Nonhuman primate models to study anxiety, emotion regulation, and psychopathology. *Ann N Y Acad Sci* 1008:189–200.
15. Oler JA, Fox AS, Shelton SE, Rogers J, Dyer TD, Davidson RJ, et al. (2010): Amygdalar and hippocampal substrates of anxious temperament differ in their heritability. *Nature* 466:864–868.
16. Hettema JM, Neale MC, Kendler KS (2001): A review and meta-analysis of the genetic epidemiology of anxiety disorders. *Am J Psychiatry* 158:1568–1578.
17. Janak PH, Tye KM (2015): From circuits to behaviour in the amygdala. *Nature* 517:284–292.
18. Fox AS, Oler JA, Tromp DPM, Fudge JL, Kalin NH (2015): Extending the amygdala in theories of threat processing. *Trends Neurosci* 38:319–329.
19. Alheid GF, Heimer L (1988): New perspectives in basal forebrain organization of special relevance for neuropsychiatric disorders: The striatopallidal, amygdaloid, and corticopetal components of substantia innominata. *Neuroscience* 27:1–39.
20. Fadok JP, Markovic M, Tovote P, Luthi A (2018): New perspectives on central amygdala function. *Curr Opin Neurobiol* 49:141–147.
21. Viviani D, Charlet A, van den Burg E, Robinet C, Hurni N, Abatis M, et al. (2011): Oxytocin selectively gates fear responses through distinct outputs from the central amygdala. *Science* 333:104–107.
22. Fadok JP, Krabbe S, Markovic M, Courtin J, Xu C, Massi L, et al. (2017): A competitive inhibitory circuit for selection of active and passive fear responses. *Nature* 542:96–100.
23. Petrovich GD, Swanson LW (1997): Projections from the lateral part of the central amygdalar nucleus to the postulated fear conditioning circuit. *Brain Res* 763:247–254.
24. Veening JG, Swanson LW, Sawchenko PE (1984): The organization of projections from the central nucleus of the amygdala to brainstem sites involved in central autonomic regulation: A combined retrograde transport-immunohistochemical study. *Brain Res* 303:337–357.
25. Oler JA, Tromp DP, Fox AS, Kovner R, Davidson RJ, Alexander AL, et al. (2017): Connectivity between the central nucleus of the amygdala and the bed nucleus of the stria terminalis in the non-human primate: Neuronal tract tracing and developmental neuroimaging studies. *Brain Struct Funct* 222:21–39.
26. Dong HW, Petrovich GD, Swanson LW (2001): Topography of projections from amygdala to bed nuclei of the stria terminalis. *Brain Res Brain Res Rev* 38:192–246.
27. Kim SY, Adhikari A, Lee SY, Marshel JH, Kim CK, Mallory CS, et al. (2013): Diverging neural pathways assemble a behavioural state from separable features in anxiety. *Nature* 496:219–223.
28. Kalin NH, Shelton SE, Davidson RJ (2004): The role of the central nucleus of the amygdala in mediating fear and anxiety in the primate. *J Neurosci* 24:5506–5515.
29. Kalin NH, Shelton SE, Davidson RJ, Kelley AE (2001): The primate amygdala mediates acute fear but not the behavioral and physiological components of anxious temperament. *J Neurosci* 21:2067–2074.
30. Amaral DG, Price JL, Pitkänen A, Carmichael ST (1993): Anatomical organization of the primate amygdaloid complex. In: Aggleton JP, editor. *The Amygdala: Neurobiological Aspects of Emotion, Memory, and Mental Dysfunction*. New York: Wiley-Liss, 1–66.
31. De Olmos JS (2004): The amygdala. In: Paxinos G, Mai JK, editors. *The Human Nervous System*, 2nd ed. San Diego: Elsevier Academic Press, 739–860.
32. Haubensak W, Kunwar PS, Cai H, Ciocchi S, Wall NR, Ponnusamy R, et al. (2010): Genetic dissection of an amygdala microcircuit that gates conditioned fear. *Nature* 468:270–276.
33. Pomrenze MB, Tovar-Diaz J, Blasio A, Maiya R, Giovanetti SM, Lei K, et al. (2019): A corticotropin releasing factor network in the extended amygdala for anxiety. *J Neurosci* 39:1030–1043.
34. Asok A, Draper A, Hoffman AF, Schukin J, Lupica CR, Rosen JB (2018): Optogenetic silencing of a corticotropin-releasing factor pathway from the central amygdala to the bed nucleus of the stria terminalis disrupts sustained fear. *Mol Psychiatry* 23:914–922.
35. Ahrens S, Wu MV, Furlan A, Hwang GR, Paik R, Li H, et al. (2018): A central extended amygdala circuit that modulates anxiety. *J Neurosci* 38:5567–5583.
36. Yu K, Ahrens S, Zhang X, Schiff H, Ramakrishnan C, Fenno L, et al. (2017): The central amygdala controls learning in the lateral amygdala. *Nat Neurosci* 20:1680–1685.
37. LeDoux JE, Cicchetti P, Xagoraris A, Romanski LM (1990): The lateral amygdaloid nucleus: Sensory interface of the amygdala in fear conditioning. *J Neurosci* 10:1062–1069.
38. Li H, Penzo MA, Taniguchi H, Kopec CD, Huang ZJ, Li B (2013): Experience-dependent modification of a central amygdala fear circuit. *Nat Neurosci* 16:332–339.
39. Ye J, Veinante P (2019): Cell-type specific parallel circuits in the bed nucleus of the stria terminalis and the central nucleus of the amygdala of the mouse. *Brain Struct Funct* 224:1067–1095.

40. Funk CM, Peelman K, Bellesi M, Marshall W, Cirelli C, Tononi G (2017): Role of somatostatin-positive cortical interneurons in the generation of sleep slow waves. *J Neurosci* 37:9132–9148.
41. Fox AS, Oler JA, Shelton SE, Nanda SA, Davidson RJ, Roseboom PH, et al. (2012): Central amygdala nucleus (Ce) gene expression linked to increased trait-like Ce metabolism and anxious temperament in young primates. *Proc Natl Acad Sci U S A* 109:18108–18113.
42. Zimin AV, Cornish AS, Maudhoo MD, Gibbs RM, Zhang X, Pandey S, et al. (2014): A new rhesus macaque assembly and annotation for next-generation sequencing analyses. *Biol Direct* 9:20.
43. Love MI, Huber W, Anders S (2014): Moderated estimation of fold change and dispersion for RNA-seq data with DESeq2. *Genome Biol* 15:550.
44. Mi H, Muruganujan A, Ebert D, Huang X, Thomas PD (2018): PANTHER version 14: More genomes, a new PANTHER GO-slim and improvements in enrichment analysis tools. *Nucleic Acids Res* 47:D419–D426.
45. Shackman AJ, Fox AS, Oler JA, Shelton SE, Davidson RJ, Kalin NH (2013): Neural mechanisms underlying heterogeneity in the presentation of anxious temperament. *Proc Natl Acad Sci U S A* 110:6145–6150.
46. Wang WJ, Tay HG, Soni R, Perumal GS, Goll MG, Macaluso FP, et al. (2013): CEP162 is an axoneme-recognition protein promoting ciliary transition zone assembly at the cilia base. *Nat Cell Biol* 15:591–601.
47. Munoz-Estrada J, Lora-Castellanos A, Meza I, Alarcon Elizalde S, Benitez-King G (2018): Primary cilia formation is diminished in schizophrenia and bipolar disorder: A possible marker for these psychiatric diseases. *Schizophr Res* 195:412–420.
48. Wang Z, Phan T, Storm DR (2011): The type 3 adenylyl cyclase is required for novel object learning and extinction of contextual memory: Role of cAMP signaling in primary cilia. *J Neurosci* 31:5557–5561.
49. Amador-Arjona A, Elliott J, Miller A, Ginbey A, Pazour GJ, Enikolopov G, et al. (2011): Primary cilia regulate proliferation of amplifying progenitors in adult hippocampus: Implications for learning and memory. *J Neurosci* 31:9933–9944.
50. Berbari NF, Malarkey EB, Yazdi SM, McNair AD, Kippe JM, Croyle MJ, et al. (2014): Hippocampal and cortical primary cilia are required for aversive memory in mice. *PLoS One* 9:e106576.
51. Duman RS, Li N (2012): A neurotrophic hypothesis of depression: Role of synaptogenesis in the actions of NMDA receptor antagonists. *Philos Trans R Soc Lond B Biol Sci* 367:2475–2484.
52. Newton AC (2010): Protein kinase C: Poised to signal. *Am J Physiol Endocrinol Metab* 298:E395–E402.
53. Amano T, Amir A, Goswami S, Pare D (2012): Morphology, PKC δ expression, and synaptic responsiveness of different types of rat central lateral amygdala neurons. *J Neurophysiol* 108:3196–3205.
54. Cassel MD, Gray TS (1989): Morphology of peptide immunoreactive neurons in the rat central nucleus of the amygdala. *J Comp Neurol* 281:320–333.
55. Cui Y, Lv G, Jin S, Peng J, Yuan J, He X, et al. (2017): A central amygdala-substantia innominata neural circuitry encodes aversive reinforcement signals. *Cell Rep* 21:1770–1782.
56. Yu K, Garcia da Silva P, Albeau DF, Li B (2016): Central amygdala somatostatin neurons gate passive and active defensive behaviors. *J Neurosci* 36:6488–6496.
57. Turner CA, Clinton SM, Thompson RC, Watson SJ Jr, Akil H (2011): Fibroblast growth factor-2 (FGF2) augmentation early in life alters hippocampal development and rescues the anxiety phenotype in vulnerable animals. *Proc Natl Acad Sci U S A* 108:8021–8025.
58. Fox AS, Souaiaia T, Oler JA, Kovner R, Kim JMH, Nguyen J, et al. (2019): Dorsal Amygdala Neurotrophin-3 Decreases Anxious Temperament in Primates. *Biol Psychiatry* 86:881–889.
59. Price JL, Russchen FT, Amaral DG (1987): The limbic region: II. The amygdaloid complex. In: Hokfelt BT, Swanson LW, editors. *Handbook of Chemical Neuroanatomy*. Amsterdam: Elsevier, 279–381.
60. Roberts GW, Woodhams PL, Polak JM, Crow TJ (1982): Distribution of neuropeptides in the limbic system of the rat: The amygdaloid complex. *Neuroscience* 7:99–131.
61. McCullough KM, Morrison FG, Hartmann J, Carlezon WA Jr, Ressler KJ (2018): Quantified coexpression analysis of central amygdala subpopulations. *eNeuro* 5:ENEURO.0010-18.2018.
62. Kim J, Zhang X, Muralidhar S, LeBlanc SA, Tonegawa S (2017): Basolateral to central amygdala neural circuits for appetitive behaviors. *Neuron* 93:1464–1479.e5.
63. Han W, Tellez LA, Rangel MJ Jr, Motta SC, Zhang X, Perez IO, et al. (2017): Integrated control of predatory hunting by the central nucleus of the amygdala. *Cell* 168:311–324.e18.
64. Amaral DG, Avendano C, Benoit R (1989): Distribution of somatostatin-like immunoreactivity in the monkey amygdala. *J Comp Neurol* 284:294–313.
65. Kovner R, Fox AS, French DA, Roseboom PH, Oler JA, Fudge JL, et al. (2019): Somatostatin gene and protein expression in the non-human primate central extended amygdala. *Neuroscience* 400:157–168.
66. Cassell MD, Gray TS, Kiss JZ (1986): Neuronal architecture in the rat central nucleus of the amygdala: A cytological, hodological, and immunocytochemical study. *J Comp Neurol* 246:478–499.
67. Martin LJ, Powers RE, Dellovade TL, Price DL (1991): The bed nucleus-amygdala continuum in human and monkey. *J Comp Neurol* 309:445–485.
68. Cai H, Haubensak W, Anthony TE, Anderson DJ (2014): Central amygdala PKC- δ (+) neurons mediate the influence of multiple anorexigenic signals. *Nat Neurosci* 17:1240–1248.
69. Lubieniecka JM, de Brujin DRH, Su L, van Dijk AHA, Subramanian S, van de Rijn M, et al. (2008): Histone deacetylase inhibitors reverse SS18-SSX-mediated polycomb silencing of the tumor suppressor—early growth response 1—in synovial sarcoma. *Cancer Res* 68:4303–4310.
70. Tang L, Nogales E, Ciferri C (2010): Structure and function of SWI/SNF chromatin remodeling complexes and mechanistic implications for transcription. *Prog Biophys Mol Biol* 102:122–128.
71. Elbau IG, Cruceanu C, Binder EB (2019): Genetics of resilience: Gene-by-environment interaction studies as a tool to dissect mechanisms of resilience. *Biol Psychiatry* 86:433–442.
72. Pruski M, Lang B (2019): Primary cilia—An underexplored topic in major mental illness. *Front Psychiatry* 10:104.
73. Ciocchi S, Herry C, Grenier F, Wolff SB, Letzkus JJ, Vlachos I, et al. (2010): Encoding of conditioned fear in central amygdala inhibitory circuits. *Nature* 468:277–282.
74. Gray TS, Magnuson DJ (1992): Peptide immunoreactive neurons in the amygdala and the bed nucleus of the stria terminalis project to the midbrain central gray in the rat. *Peptides* 13:451–460.
75. Moga MM, Gray TS (1985): Evidence for corticotropin-releasing factor, neurotensin, and somatostatin in the neural pathway from the central nucleus of the amygdala to the parabrachial nucleus. *J Comp Neurol* 241:275–284.
76. Rankin SL, Guy CS, Rahimtula M, Mearrow KM (2008): Neurotrophin-induced upregulation of p75NTR via a protein kinase C-delta-dependent mechanism. *Brain Res* 1217:10–24.
77. Kanehisa M, Goto S (2000): KEGG: Kyoto Encyclopedia of Genes and Genomes. *Nucleic Acids Res* 28:27–30.
78. Kanehisa M, Sato Y (2020): KEGG Mapper for inferring cellular functions from protein sequences. *Protein Sci* 29:28–35.
79. Greene MW, Morrice N, Garofalo RS, Roth RA (2004): Modulation of human insulin receptor substrate-1 tyrosine phosphorylation by protein kinase C δ . *Biochem J* 378:105–116.
80. Pare D, Smith Y (1993): The intercalated cell masses project to the central and medial nuclei of the amygdala in cats. *Neuroscience* 57:1077–1090.
81. Gungor NZ, Yamamoto R, Pare D (2015): Optogenetic study of the projections from the bed nucleus of the stria terminalis to the central amygdala. *J Neurophysiol* 114:2903–2911.
82. Gray TS, Cassell MD, Williams TH (1982): Synaptology of three peptidergic neuron types in the central nucleus of the rat amygdala. *Peptides* 3:273–281.
83. Paxinos G, Huang X, Petrides M, Toga AW (2009): *The Rhesus Monkey Brain: Stereotaxic Coordinates*. San Diego: Elsevier.
84. Schindelin J, Arganda-Carreras I, Frise E, Kaynig V, Longair M, Pietzsch T, et al. (2012): Fiji: An open-source platform for biological-image analysis. *Nat Methods* 9:676–682.

Transcriptional Profiling of Primate Central Nucleus of the Amygdala Neurons to Understand the Molecular Underpinnings of Early Life Anxious Temperament

Supplement 1

Supplemental Methods

Animals

All animals were phenotyped for AT as described below and brains for the subset of 47 animals were collected for LCM and RNA-Seq analysis. The majority of these 47 animals were of Indian ancestry, with a subset that were a hybrid of Indian and Chinese ancestry. Monkeys were humanely euthanized by anesthetizing with ketamine (at least 15 mg/kg, IM) followed by sodium pentobarbital. Two C57BL/6J mice, two KO; B6;129X1-*Prkcd*^{tm1Msg}/J mice, and two additional rhesus monkey brains were used to characterize antibodies. Triple-labeling immunofluorescence and stereology was performed on three C57BL/6J mice (WT, age=p21) and three rhesus monkey brains (average age=3.1 yrs). Triple-labeling immunofluorescence for the retrograde traced issue was performed on six monkeys (*Macaca fascicularis* and *Macaca nemestrina*; average age=2-3 years). All procedures were approved by the Committee on the Ethics of Animal Research of the University of Wisconsin and of the University of Rochester.

Animal Housing

Veterinary care, supported by clinical laboratories, was available at both the Wisconsin National Primate Center and the Harlow Center for Biological Psychology, as well as the University of Rochester 24 hours a day, seven days a week. Monkeys were mother-reared, and pair-housed in a room containing multiple cages, to facilitate social housing. Monkeys experienced a 12-hour light/dark cycle, received food 1-2 times per day and water was available *ad libitum*. Monkeys experienced enrichment activities such as toys, foraging devices, tactile devices, audio, television and snack foods such as fruit at least once per day. Mice were ordered from The Jackson Laboratory (Bar Harbor, ME) and were group housed at the Wisconsin Psychiatric Institute and Clinics for at least 7 days before experimentation. Mice experienced a 12-hour light/dark cycle and were given *ad libitum* access to food and water. Any discomfort, distress, pain, and injury were minimized by the appropriate use of anesthetic and analgesic drugs under the direction and supervision of the veterinary staff.

Anxious Temperament Phenotyping

Anxious temperament (AT) phenotyping was performed between 8:00am and 11:00am to control for time of day. To assess individual differences in AT, we used the mildly threatening no eye contact condition (NEC) of the human intruder paradigm (Figure S1A; 1-4) During this 30 minute condition, a human intruder presents their profile to the monkey ensuring to not make eye contact (2, 4). This condition is unique in that it elicits behaviors that reflect uncertainty in relation to potential threat. High levels of AT are characterized by increased plasma cortisol, increased freezing, and decreased cooing occurring during the NEC condition (4). Freezing is defined as a 3 second period characterized by lack of body movement that is accompanied by a tense body posture and sometimes slow movements of the head. Coo vocalizations are vocalizations made by rounding and pursing the lips characterized by an increase, then decrease in frequency and intensity. The duration of freezing was assessed for six consecutive 5-minute blocks. The average freezing duration across the blocks was log transformed to ensure a normal distribution. Cooing frequency was similarly averaged across the blocks and square root transformed. Blood samples

for cortisol assessment were collected by femoral venipuncture at the end of the 30-minute NEC exposure. Blood withdrawal was collected when monkeys were placed in a special cage used to limit their locomotor capacities and a leg could be accessed for venipuncture. FDG PET imaging was performed at the end of the NEC period but is not included in this paper. Because cortisol is affected by time of day, cortisol levels were residualized for the time of day of sample collection. Freezing, cooing and cortisol were also residualized for age. For the 47 animals, AT scores were calculated by taking the average of their combined residualized and standardized freezing, cooing, and cortisol values. When examining the AT scores of these 47 animals in relation to the larger superset, we found that they had a similar distribution, spanning approximately +/- 1 std from the mean of the larger cohort (Figure S1B). Behavioral data was analyzed using scripts written in python 3.6 (Python Software Foundation, <https://www.python.org/>) using IPython (5) that utilized pandas (6), scipy (7), and statsmodels (8) modules.

Cortisol Assessment

Plasma samples were assayed for cortisol in duplicate using the DPC Coat-a-count radioimmunoassay (Siemens, Los Angeles, CA). The inter-assay CV%'s calculated for a low and a high control were based on 21 assays. The low control had an average value of 48.4 µg/dL and a CV% of 7.0 and the high control had an average value of 128.3 µg/dL and a CV% of 7.0. The limit of detection defined by the lowest standard was 1 µg/dL.

NeuN Rapid Staining Protocol

Brain slabs used for laser capture microdissection (LCM) were counterbalanced for hemisphere across animals. The slab containing the CeL was selected for each animal. Acetylcholinesterase (AChE) staining was used to confirm that the slab contained the amygdala (Figure S2B). In cases in which the amygdala was contained in two slabs, both were used. Tissue was sectioned on a cryostat, mounted on LCM slides, and placed in a -80°C freezer until staining. All staining was completed in an RNA-free environment and all steps were done on ice unless otherwise specified. LCM slides were removed from the -80°C freezer and thawed on a metal block for 30 seconds. Slides were fixed in acetone for 3 minutes at -20°C and then washed in PBS with 0.1% Triton x-100 (PBS-T) for 2 minutes. The tissue was stained with a neuron specific protein (NeuN) antibody (MAB377, Millipore, Burlington, MA) at a 1:200 dilution for 25 minutes at room temperature. Slides were submerged in PBS-T for 2 minutes and incubated in an HRP secondary antibody (PI-2000, Vectorlabs, Burlingame, CA) at 1:250 for 30 minutes at room temperature. Slides were then washed in PBS-T for 2 minutes and dipped in regular PBS for 30 seconds. Tissue was incubated in ImmPACT VIP peroxidase substrate (SK-4605, Vectorlabs) for 7-10 minutes before washing in DEPC-treated H₂O for 5 minutes. Finally, the slides were dipped into 95% ethanol briefly before being dehydrated for 10-20 seconds each in 95% ethanol, 100% ethanol, and xylene. Slides were dried in a fume hood for 5 minutes before being transported to the laser capture microscope.

Laser Capture Microdissection Protocol

For dissection, neurons were identified at 20x magnification and a circle that was approximately 850 µm² was drawn around each neuron and neurons were then dissected with a laser and fell into the lid of a microfuge tube (PCR-05-C, Axygen, Corning, NY) filled with 40uL of lysis buffer. After all neurons from the slide were captured, an additional 10uL of lysis buffer was added to the microfuge tube. The tube was vortexed on high for 30 seconds before being placed on dry ice. Tubes containing neuronal RNA were only used if at least 80% of the cells captured were identified as coming from the CeL, confirmed by overlaying each LCM slide image with its adjacent AChE slide. From our collection, we established 3 categories: 100% CeL cells, 80-99% CeL cells, and <80% CeL cells. Those slides that were <80% CeL cells were not used for RNA-Seq. To determine the "CeL neuron accuracy" for each animal, we calculated the proportion of the number of slides that contained 80-99% of CeL neurons out of total slides used for RNA-Seq (X 80-99%

slides / (X 80-99% slides + Y 100% slides); Figure S3B). AChE images were assigned a bregma value that most closely matched that AchE image in the Paxinos Atlas (9). A “weighted average bregma” value was calculated for each animal by multiplying the bregma value for each slide by the number of cells captured for in that slide and taking an average (Figure S3B). For half of the animals (n=29), RNA from one slide was extracted and run on an Agilent Bioanalyzer to determine 18S and 28S peaks and RNA integrity numbers (average = 4, std = 0.75).

RNA Sequencing Data Analysis

All data were analyzed using either scripts written in python or R. OLS regression and permutation testing were performed in python 2.7. For DESeq2 analyses, data were manually filtered and outliers removed based on a cook's D distance of 3.8, calculated using a quantile function (qf) distribution as recommended by DESeq2 (10). For the heatmap (Figure 2A), the ward method of unsupervised clustering was performed using scripts written in python 3.6 (Python Software Foundation, <https://www.python.org/>) using the seaborn (version 0.0.9, <https://seaborn.pydata.org>) module which utilizes matplotlib (11). Gene expression values in the heatmap are presented as log2 transformed, min-max scaled values. Gene expression values in scatterplots are quantile normalized, log2 transformed, and residualized for covariates.

Non-parametric Multiple Testing Correction

For each gene, a permutation test was performed to obtain a non-parametric empirical p-value for the squared value of the correlation coefficient between AT and the log-transformed residualized value from our model covariates (age and accuracy ratio). In each simulation the AT parameter was shuffled, and the correlation coefficient was calculated and compared to our real correlation coefficient value. The simulation was carried out until the null squared correlation exceeded the observed parameter at least ten times (a numerator of between 10,000 and 30 million iterations), and this value was used to calculate the empirical p-value. Empirical p-values were then FDR corrected using the Benjamin-Hochberg procedure.

Weight Gene Co-expression Network Analysis

Iterative weighted gene co-expression network analysis (iWGCNA) was performed to identify groups of related genes that may fall within the same molecular pathway (12). CeL LCM transcripts were limited to those expressed in at least 50% of animals with a minimum expression level of 10 transcripts for those animals expressing the gene. Gene expression values were correlated and then taken to a power β to reach approximate scale-free topology. This was determined using the WGCNA package in R (13) and was found to be 10. Signed co-expression networks were constructed that had a minimum module size of 15 genes and a minimum kME value of 0.4. Genes that did not form strong associations with other genes were considered unclassified and were removed from further analyses. Modules were tested to determine whether they were significantly related to AT or its components using a model that included CeL neuron accuracy and age at ToD as covariates and p-values were FDR corrected. All analyses were written in python 3.6 (Python Software Foundation, <https://www.python.org/>) using scipy, seaborn (version 0.0.9, <https://seaborn.pydata.org>), matplotlib (11), and pandas (7).

Immunohistochemistry: Tissue collection, PKC δ antibody characterization, staining protocols, and stereological analysis

To characterize the PKC δ antibodies, a brain from one additional monkey and brains from a wildtype (WT; C57BL/6J; stock 000664, Jackson Laboratories, Farmington, CT) and a PKC δ knockout (KO; B6;129X1-*Prkcd*^{tm1Msg}/J; stock 028055, Jackson Laboratories) mouse were used. After characterization, perfused brains from three monkeys and three mice were used for between species comparison of PKC δ in the CeL. Animals were perfused using a standard protocol (15). Brains were extracted, fixed overnight in 4% paraformaldehyde, cryoprotected in 30% sucrose,

sectioned at 40-50 μ m and stored in cryoprotectant solution (30% ethylene glycol and 30% sucrose in 0.1 M phosphate buffer) at -20 °C (16).

PKC δ Antibody Characterization for Use in Rhesus Monkey Tissue

Three PKC δ antibodies (Key Resources) were assessed by staining both WT and PKC δ KO tissue using a standard immunohistochemistry protocol (see below). Those antibodies with specific binding to the PKC δ protein were used in subsequent immunofluorescence experiments (Figure S4). The same antibodies were used to test for PKC δ staining in the monkey. To characterize specificity of PKC δ in monkey tissue, each antibody was preabsorbed with PKC δ peptide. Ten-fold molar excess of the PKC δ purified peptide was added to each antibody at their respective dilutions (Key Resources). The antibody-antigen mixture incubated for 36 hours at 4°C with mild agitation. The mixture was spun at 16,000g for 30 minutes. The resulting supernatant was pipetted into a clean vial and used in place of the primary antibody in the immunohistochemistry protocol.

Immunohistochemistry Protocol

Tissue from one mouse and monkey were stained together and all tissue was stained using the same lot of antibodies (Key Resources) and blocking serums. All tissue was removed from cryoprotectant solution 24 hours before staining and rinsed at least 3 times in 1x PBS. Primary antibodies were diluted in 1x PBS with 0.3% Triton x-100 and tissue was incubated overnight at room temperature. All secondary antibodies were made in 5% donkey serum. Fluorescent antibodies were also filtered through a 0.45 μ m filter to improve background staining.

Antibody characterization experiments were completed first and all staining was visualized using 3,3'-Diaminobenzidine (DAB). Tissue was incubated in 5% donkey serum (017-000-121, Jackson ImmunoResearch Laboratories, West Grove, PA) for 1 hour at room temperature. Tissue was subsequently washed three times in 1x PBS before being placed in PKC δ antibody overnight at room temperature. The following day, tissue for the antibody characterization experiments was washed in 1x PBS and incubated in an HRP conjugated secondary antibody diluted with blocking serum at 1:250 for 1 hour at room temperature. Tissue was then washed and incubated with ImmunoPact DAB (SK-4105, Vector Laboratories) for visualization of staining. Tissue was then mounted, left to dry overnight and then dehydrated in 75%, 95%, 100% ethanol solutions and xylene before being cover slipped. Images were captured at 1.25x, 5x and 20x magnification on a Leica LMD6500 microscope.

For triple labeling immunofluorescence, tissue was incubated serially in each antibody to avoid background staining. The staining protocols for the tissue used in the NeuN, PKC δ , and SST triple labeling experiment and the tissue used in the retrograde tracing experiment were the same. For the stereology experiment, tissue was first incubated in NeuN antibody overnight at room temperature, followed by three 1x PBS washes and AlexaFluor 647 donkey anti-mouse secondary incubation for 1 hour at room temperature. For the retrograde tracing experiment, tissue was first incubated in anti-rhodamine, anti-WGA, or anti-fluorescein antibody overnight at room temperature, followed by three 1x PBS washes and AlexaFluor 568 donkey anti-mouse secondary or AlexaFluor 488 donkey anti-goat secondary incubation for 1 hour at room temperature. Tissue was rinsed three times in 1x PBS and incubated in PKC δ antibody (1:200, Thermo Fisher) at room temperature for 24 hours for the mouse tissue and 48 hours for the monkey tissue. The following day, tissue was washed three times in 1x PBS, incubated in AlexaFluor 488 donkey anti-rabbit for 1 hour at room temperature, washed three times in 1x PBS, and incubated in SST primary antibody for 72 hours to improve antibody penetration through the tissue. On the final day of staining, tissue was washed three times in 1x PBS and incubated in AlexaFluor 568 donkey anti-goat for 1 hour at room temperature before being washed in 1x PBS, incubated for 5 minutes in

DAPI, mounted on slides, and coverslipped with Prolong Gold AntiFade Mountant (P36930, Thermo Fisher).

Anatomical Boundaries of the Amygdala

The anatomical boundaries of the amygdala nuclei are well established in rodents (17). We delineated the lateral division of the central nucleus in mouse tissue based on previously described work (18) and corroborated this with adjacent sections stained for AChE. In rhesus monkeys the nomenclature and anatomical boundaries have been previously described (19, 20). We used these descriptions to delineate the anatomical boundary for the lateral division of the central nucleus (CeL) in the rhesus monkey. We used the nomenclature system in the Paxinos atlas (9) for rhesus monkeys (Figure 3A) and for consistency, extend this nomenclature to the mouse (Figure 3A).

Imaging Protocol and Stereological Analysis

For the NeuN, PKC δ , and SST triple labeling experiment, the optical fractionator method was used to determine the total number of neurons, PKC δ + neurons, SST+ neurons, and double labeled neurons in the CeL (21, 22). Eight to ten sections per monkey and 4 sections per mouse through the anterior-posterior extent of the CeL was used and the first section was randomly selected within the first 6 (in mouse) or 8 (in monkey) sections. Each slide that contained the CeL was imaged with a 40x oil objective with a numerical aperture of 1.3 on a Nikon A1R+ confocal microscope. Stacks were acquired with a z-step of 1.25 μ m for monkey sections and 1 μ m for mouse sections and multiple stacks were stitched to produce whole CeL stacks to be used for offline stereological counting. Nikon nd2 files were exported from NIS elements into individual .tif files. Stereological counting was done in StereoInvestigator 2018.1.1 (MBF Bioscience, Williston, VT USA).

A sampling scheme was determined to estimate PKC δ and SST expressing neurons out of total neurons with an estimated Gunderson coefficient of error of 0.1 for each cell type. Neurons were counted when the center of the nucleolus of the NeuN stain came into focus. Cells expressing SST or PKC δ were counted only if they were also double labeled with NeuN. In a pilot study, NeuN and PKC δ + neurons were counted at 25% in both species and SST+ and double labeled SST/PKC δ neurons were sampled at 100%. Using the sample-resample option in StereoInvestigator it was determined that in both species, PKC δ and NeuN labeled neurons could be sampled at a minimum of 2% and SST neurons could be sampled at a minimum of 10%. To ensure accurate counts, we chose to sample PKC δ and NeuN labeled cells at 5% and SST neurons at 20% in monkey tissue. SST/ PKC δ double labeled neurons were also sampled at 20% in monkey tissue and at 100% in mouse tissue. Section contours were determined based on CeL structure and NeuN staining and also followed the pattern visualized by adjacent AChE stained sections. For cell counting, section thickness was measured at every 10th counting site. Counting frames were set at 75 μ m x 75 μ m in both mouse and monkey because frames of this size comfortably contained 4-6 cells. Tissue shrinkage was not consistently observed, and so guard zones were set at 5 μ m which still allowed for a 30 μ m disector height. To characterize the A-P distribution of the counted cells, cell counts were divided by the sampling percentage. Counts for each marker were then divided by the number of neurons counted in that section so that they could be presented as percentages.

Overall stereological estimates for each cell type are presented as percentage of the total number of neurons estimated. Between species differences for each cell type were tested using t-tests. Within species and for each cell type, an OLS regression model was used to investigate whether A-P location predicted number of cells counted. A variable for subject was included as a covariate in this model. A separate OLS model was run to test whether the A-P distribution for each cell

type was different between species. One section from one monkey was not used as studentized residuals and cooks distance metrics demonstrated that it was an outlier. All statistical analyses were run in python 3.6 using the statsmodels (version 0.8.0) module.

Surgery Procedure and Tissue Collection for Retrograde Injections

The surgical procedure has been previously described for these animals, which were used as part of other studies (16, 23). The coordinates of the BST were localized for each animal prior to stereotaxic surgery by acquiring T2 weighted (structural) MRI images through the entire brain (3T, coronal sections, 0.8 mm thick, 0.1 mm apart). Animals were pre-anesthetized, intubated, and maintained on isofluorane throughout stereotaxic surgery for placement of injections. We placed multiple small injections (40 nL) of the bidirectional tracers, Lucifer yellow conjugated to dextran amine (LY; 10%, Molecular Probes, Eugene, OR), tetramethylrhodamine, conjugated to dextran amine ('fluororuby', FR; 4%, Molecular Probes), and fluorescein conjugated to dextran amine (FS; 10%, Molecular Probes) into the BSTL, in addition to several injections of the tracer wheat-germ agglutinin-horse radish peroxidase (WGA; 10%, Sigma, St. Louis, MO). Control injections of all tracers were placed in the nearby striatum. Previous studies from our laboratory have indicated that there is no cross-reactivity of antibodies to FR, FS, WGA and LY, permitting injections using different tracers into the same animal.

Two weeks after surgery, animals were deeply anesthetized and perfused through the heart with 0.9% saline containing 0.5 ml of heparin sulfate (200 ml/min for 10 minutes), followed by cold 4% paraformaldehyde in a 0.1 M phosphate buffer/30% sucrose solution (100 ml/min for 1 h). The brain was extracted from the skull, placed in a fixative overnight, and then put through increasing gradients of sucrose (10%, 20%, 30%). Brains were cut on a freezing microtome (40 μ m) and all sections were stored in cryoprotectant solution (30% ethylene glycol and 30% sucrose in 0.1 M phosphate buffer) at -20 °C (24). After confirmation of the injection and retrograde labeling using permanent immunostaining methods (23), additional sections through the extended amygdala for each case were selected for triple-labeling experiments.

Retrograde Tracing Imaging Protocol and Analysis

Each slide that contained the CeL was investigated for the density of retrograde-labeled cells. For cases where there were many retrograde-labeled cells, the whole CeL was imaged and multiple stacks were stitched to produce whole CeL stacks to be used for offline counting. In cases where sections only expressed a small number of retrograde-labeled cells, individual stacks centered on the labeled cells were imaged and used for offline counting. Imaging parameters and image handling matched those used above. Retrograde-labeled neurons were first counted with channels for all other markers turned off. Once retrograde-labeled neurons were counted, each channel for the other marker was added to determine co-expression. Cells identified in the top 5 μ m and bottom 5 μ m were not counted. The overlap between retrograde-labeled neurons, PKC δ , SST, and SST/ PKC δ are presented as percentages. Venn diagrams were constructed with python 3.6 using the Venn3 module.

Supplemental Results

AT Phenotyping

AT is a composite score of threat-related behavioral and pituitary-adrenal activation occurring during the potentially threatening no eye contact condition (NEC) of the human intruder paradigm (Figure S1A; 1-4). During NEC, monkeys respond by inhibiting their behavior, as characterized by increases in freezing duration and decreases in coo vocalizations. These responses are accompanied by increases in cortisol, a reflection of hypothalamic-pituitary axis activation. AT is calculated within a sample of animals as a standardized composite of NEC-induced increases in freezing duration, decreases in cooing frequency, and increases in plasma cortisol concentration (see above).

To determine whether the AT scores of the 47 animals were representative of the AT scores of a much larger population ($n=721$) from which the animals in this study were a sub-sample, AT was calculated in two ways. First, AT was determined in relation to the 47 animals used in this study and this was compared to the AT scores of these same animals when calculated with the large group of 721 animals. When examining the AT scores of the animals used in this study as calculated in relation to each other, we found that these AT scores had a similar distribution as the AT scores across the whole 721 animals. AT as calculated within the current sample ($n=47$), spanned approximately ± 1 std from the mean of the larger cohort (Figure S1B). We computed the ranks of the AT scores for the 47 animals when they were calculated the two different ways and found that the spearman correlation between the ranks was $\rho=0.7$ ($p<0.0001$). Additionally, a Wilcoxon signed-rank test demonstrated that the ranks did not significantly differ ($Z=527$, $p=0.69$). This demonstrates that the AT scores as calculated within the 47 animals reflects the range of individual differences and AT scores of those animals in the larger population.

CeL Neuronal Collection

Previous work from our laboratory demonstrated that metabolism within the Ce is significantly associated with AT (25, 26). High levels of the serotonin transporter demarcate the CeL so that by imaging the serotonin transporter with positron-emission-tomography, we were able to identify the peak correlation to be within the CeL (Figure S2A; (27). Additionally, neurotoxic lesions of the rhesus Ce result in decreased expression of AT's components (28, 29). These findings in primates, along with rodent studies, formed the basis of our focus on CeL neurons. In the present study, the CeL was identified using AChE staining. In adjacent sections used for LCM, CeL neurons were identified with a neuron-specific rapid staining protocol. This LCM approach was advantageous in specifically identifying the CeL, which changes shape and position across the A-P extent of the amygdala. These CeL neurons were individually captured and pooled, and the RNA was extracted and sequenced (Figure S2B). Across all animals, on average, 90% of the cells that were sequenced were confirmed to have been collected from the CeL, as reflected in our average bregma estimates and CeL neuron accuracy measure for each animal (Table S1, Figure S3B). Neuronal enrichment was also confirmed, as we found greater expression of neuron-specific genes compared to glia-specific genes ($t=36.4$, $p<0.0001$; Figure S3C).

AT's Transcriptomic Architecture

To expand our analyses of the transcriptomic architecture of AT as it relates to its components, we performed four separate regression analyses for each gene's expression level in relation to our phenotypic measures: AT, freezing, cooing, and cortisol. We then asked whether the t-values from each of these regressions between genes and phenotype were correlated across components and AT. Results demonstrated that significant correlations were found between the t-values characterizing the relation between expression levels and AT with the t-values for freezing (Figure S5A, $\rho=0.88$, $p<0.001$), cooing (Figure S5B, $\rho=-0.72$, $p<0.001$), and cortisol

(Figure S5C, $\rho=0.33$, $p<0.001$). When comparing gene relations among components, we also found associations between genes related to freezing with those related to cooing (Figure S5D, $\rho=-0.76$, $p<0.001$) as well as between genes associated with cortisol and cooing ($\rho=0.31$, $p<0.001$, Figure S5E). We did not observe this relationship between genes associated with freezing and cortisol (Figure S5F, $\rho=-0.02$, $p=0.27$). These data support the hypothesis that AT-related genes include component-general genes such as those that are associated with multiple components and AT rather than a single component, as well as component-specific genes, e.g. those specifically related to freezing.

Weight Gene Co-Expression Network Identifies Gene Modules Associated with AT

Seventy-five modules were identified (Figure S6A; Table S4). Of these, 16 were associated with AT and its components ($p<0.05$, uncorrected). Of these 10 were AT-related, 5 were associated with freezing, 5 with cooing, and 7 with cortisol (Figure S6B). We also found that 3 modules were AT-specific and 7 which were associated with at least one of AT's component (Figure S6C). Two CeL modules were significantly correlated with AT after multiple testing correction ($fdr<0.1$) and one of these modules was also significantly correlated with freezing (Figure S6A;). Module P1_I16_M14 has a strong negative association with AT ($R^2 = 0.5$) and a strong negative association with freezing ($R^2 = 0.47$). This module was particularly interesting because roughly half of its genes were also found to be associated with AT in our transcript analysis. Module P2_I4_M2 was also significantly and positively associated with AT ($R^2 = 0.29$) and 56% of the genes comprising this module were also independently associated with AT. Some of the genes within these modules also had high kME scores suggesting that these are “hub” genes that are highly connected to the other genes within the module (Table S4, genes with *).

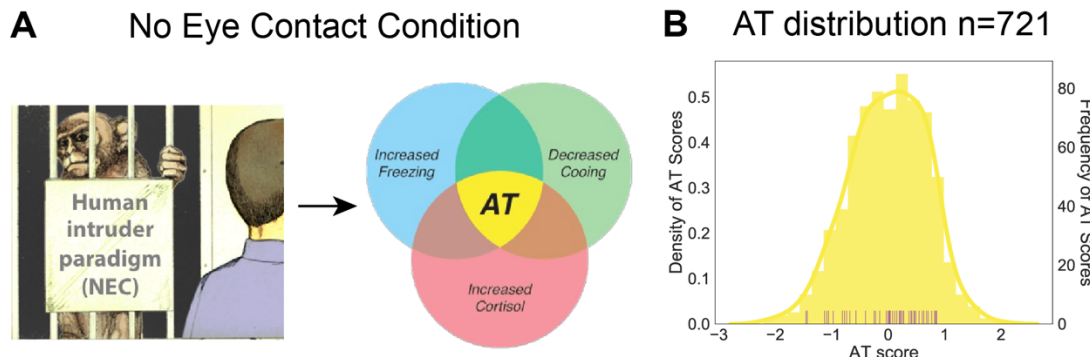
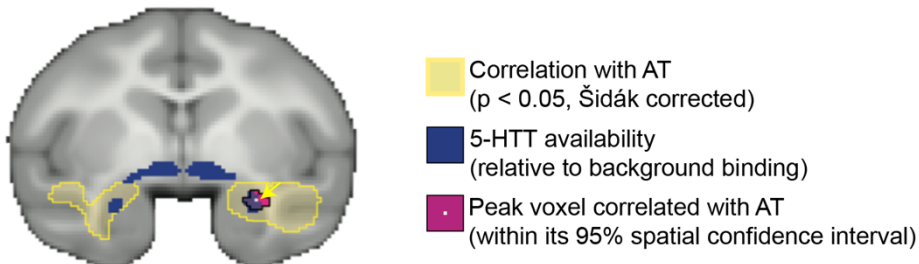


Figure S1. AT phenotype and distribution. (A) Human Intruder No-Eye Contact condition elicits behavioral and physiological responses associated with uncertain threat such as increased freezing, decreased cooling, and increased cortisol, which together comprise the AT-phenotype. (B) Histogram of AT across a larger superset of animals ($n=721$) in yellow. The purple rugplot below demonstrates the AT scores of the animals in this study as they were calculated within this group of 47 animals.

A NEC metabolism and AT



B LCM Methods

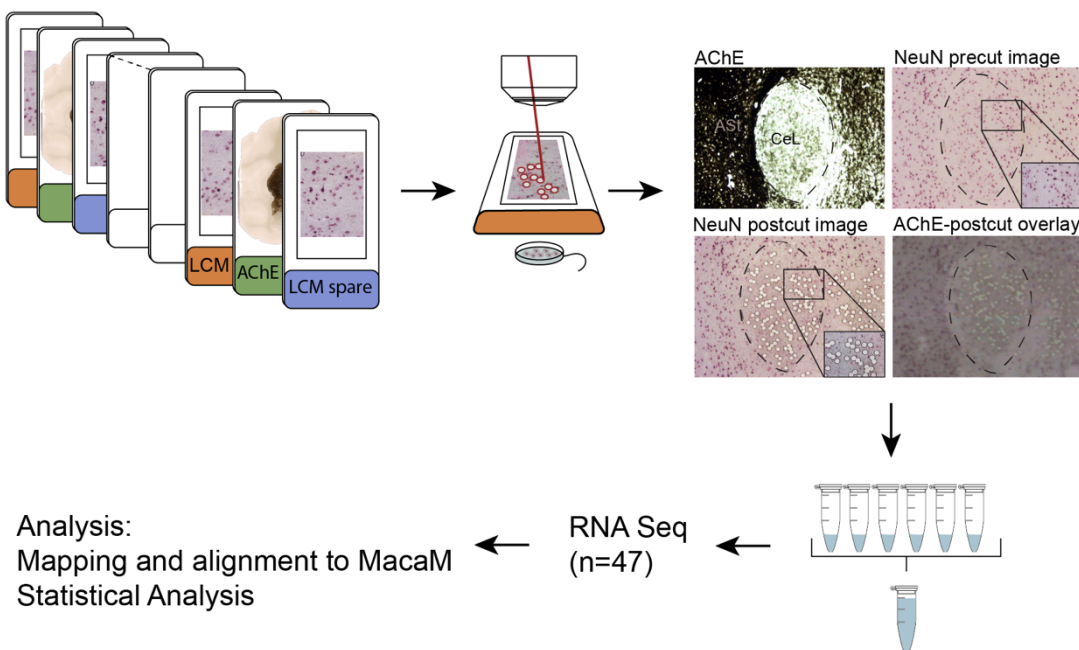


Figure S2. AT-associated PET metabolism in the Ce as a rationale for laser capture microdissection and sequencing of CeL neurons. (A) Using data from our large sample of AT-phenotyped and brain imaged animals, we previously demonstrated that individual differences in NEC-associated PET metabolism are related to individual differences in AT (yellow, (26)). We identified the peak AT voxels (pink) to be in the Ce region by demonstrating an overlap with serotonin transporter binding (blue), which, relative to surrounding regions, is elevated in the CeL. (B) Brain slabs containing the amygdala were identified and the A-P location was determined before sectioning. Tissue was sectioned and mounted on LCM slides (orange and blue labels). Adjacent slides were stained with AChE (green labels) to determine the location of the CeL. LCM slides were stained with an abbreviated NeuN protocol and CeL neurons were captured into the lid of a microfuge tube. Post-cut overlays were made for every slide to confirm capture location. RNA from 500-600 CeL neurons was pooled and used for RNA-Seq ($n=47$). Reads were processed and aligned to MacaM (30).

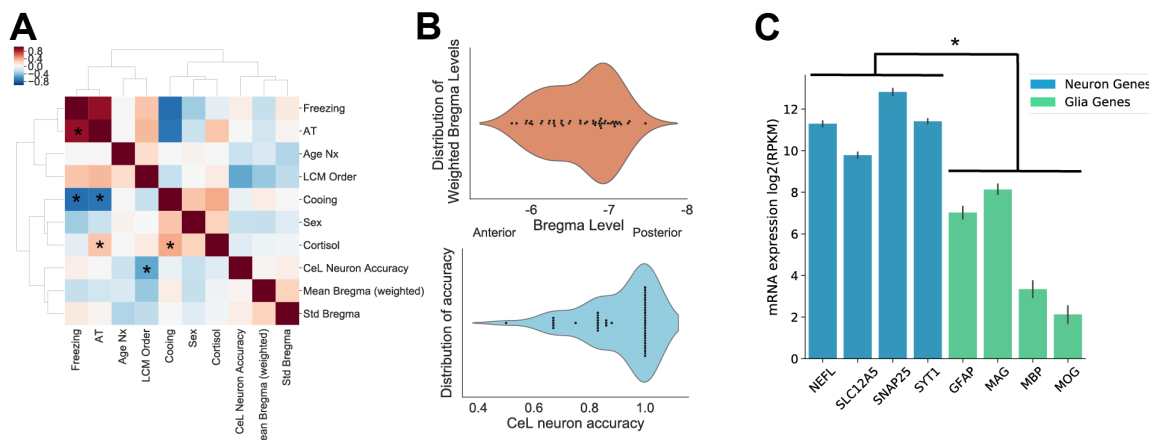


Figure S3. Characterization of LCM sampling method. (A) Heatmap depicting the Pearson correlations between model predictors (AT, freezing, cooling, and cortisol) as well as variables that were tested as covariates. Red indicates a positive correlation. Starred boxes indicate statistically significant Šidák-corrected p-values. (B) Top: Distribution of the weighted average bregma for each animal used for LCM, calculated by multiplying the bregma value of each slide by the number of cells captured in that slide and taking an average for each animal. Bottom: Distribution of CeL neuron accuracy for each animal, calculated as the proportion of the number of slides that contained 80-99% of CeL neurons out of total slides used for RNA-Seq for that animal. (C) Reads per kilobase million (RPKM) normalized mRNA expression values for neuron (blue) and glia (green) associated genes. Neuronal LCM samples expressed on average a greater amount of neuron-specific gene expression than glia-specific gene expression ($p<0.0001$, $t=36.4$; t-test). Error bars are displayed as SEM.

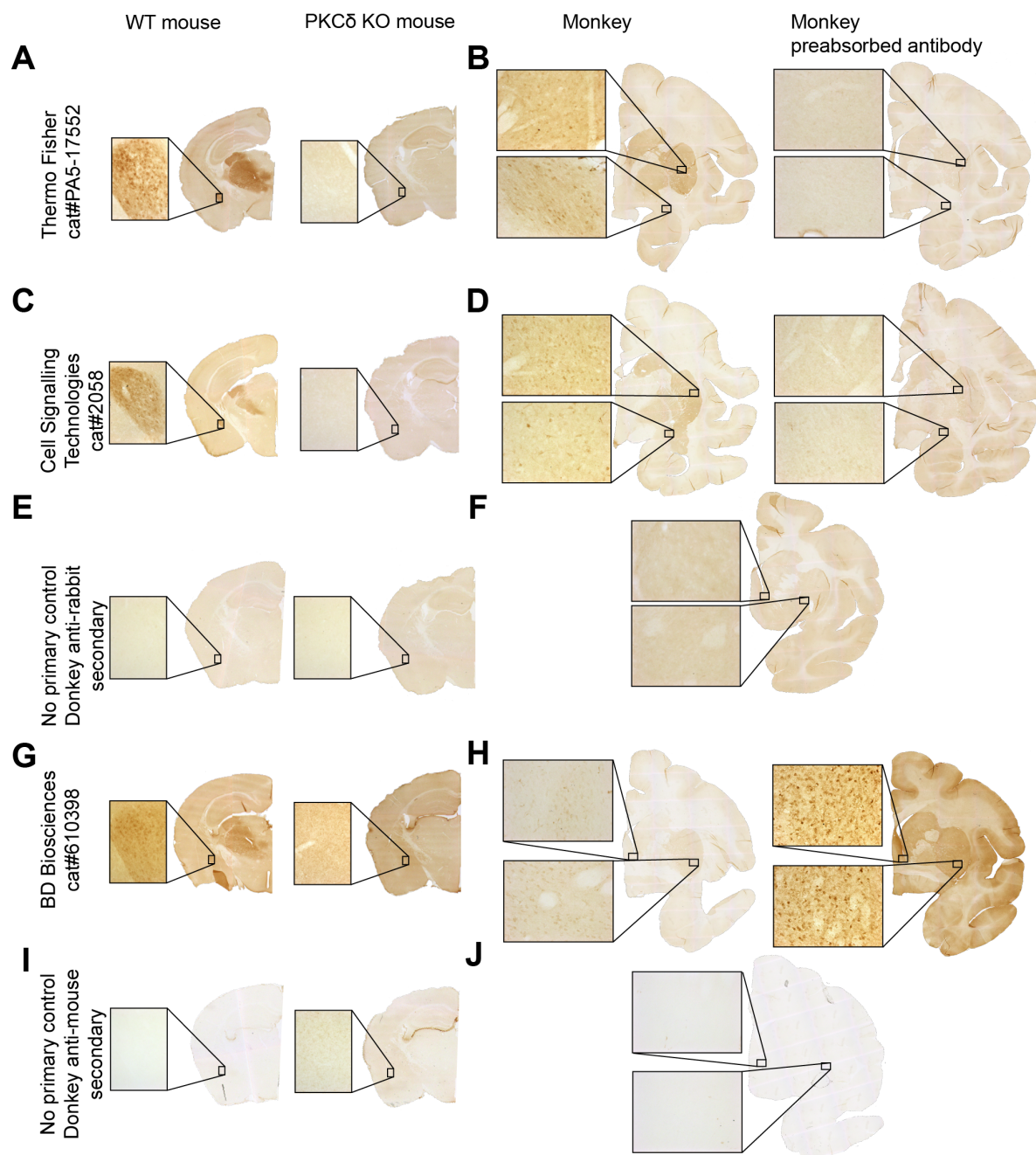


Figure S4. Characterization of PKC δ antibodies. Columns: Wild Type Mouse tissue, PKC δ Knock Out Tissue, Monkey tissue stained with PKC δ antibody, Monkey tissue stained with preabsorbed antibody. Rows: (A-B) ThermoFisher anti-PKC δ antibody, (C-D) Cell Signaling Technology anti-PKC δ antibody, (E-F) Donkey anti-rabbit secondary only control, (G-H) BD Biosciences anti-PKC δ antibody, (I-J) Donkey anti-mouse secondary only control. ThermoFisher and Cell Signaling Technology anti-PKC δ antibodies gave the most robust staining in both monkey and mouse tissue.

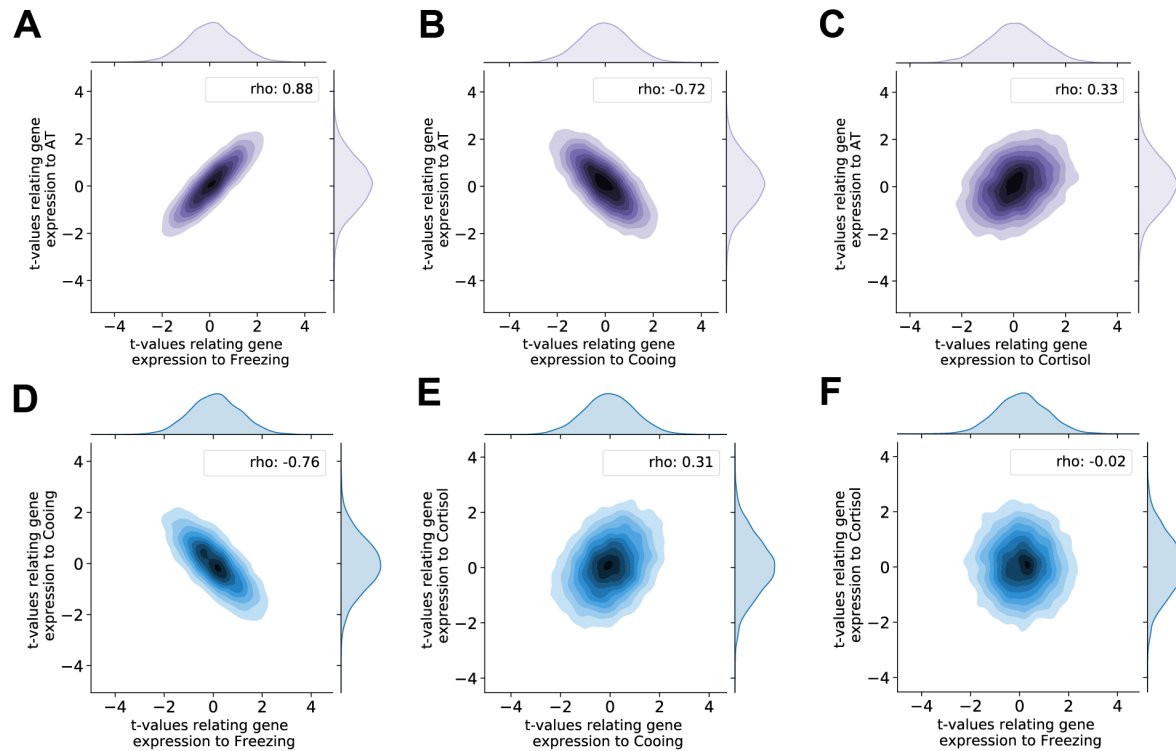


Figure S5. AT components share a molecular substrate. Kernel density plots depicting the distribution of t-values and Spearman correlations between t-values relating gene expression to (A) AT and freezing ($\rho=0.88$, $p<0.001$) (B) AT and cooing ($\rho=-0.72$ $p<0.001$) (C) AT and cortisol ($\rho=0.33$, $p<0.001$) (D) cooing and freezing ($\rho=-0.76$, $p<0.001$) (E) cortisol and cooing ($\rho=0.31$, $p<0.001$) (F) cortisol and freezing ($\rho=-0.02$, $p=0.27$). Reported p-values are Šidák corrected.

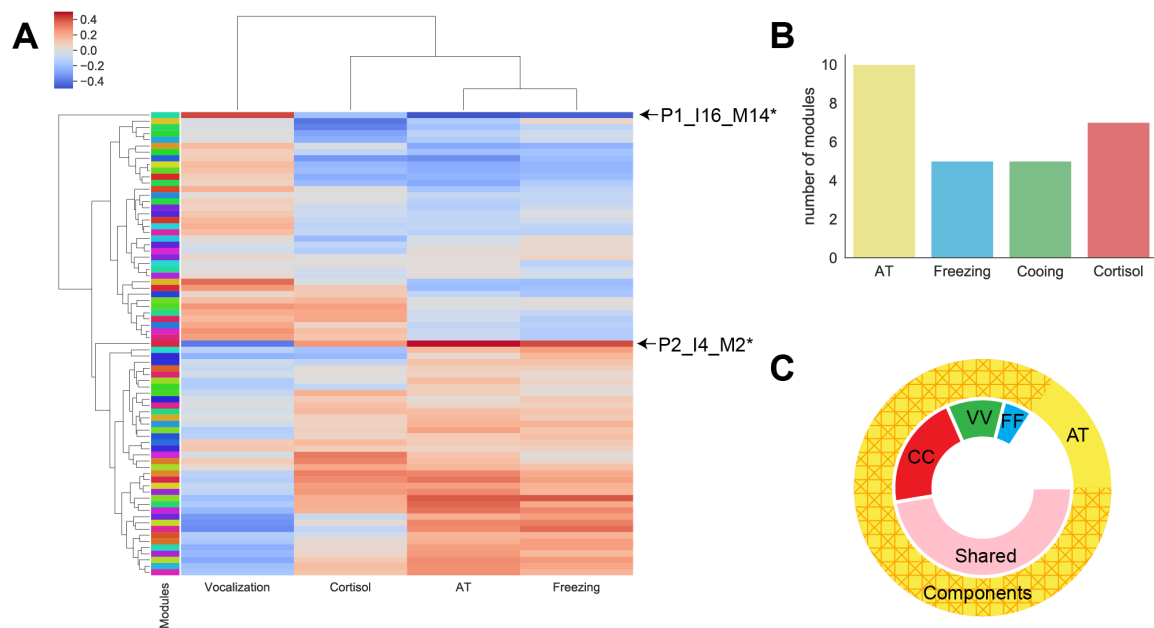


Figure S6. WGCNA modules associated with AT and its components. (A) Heatmap depicting the pearson's correlation between each WGCNA module and AT and its components. Red colors indicate positive correlations and blue colors indicate negative correlations. Two modules (P1_I16_M14 and P2_I4_M2) were significantly associated with AT and passed multiple comparison correction ($fdr < 0.1$). (B) Barplot demonstrating that AT is associated with a greater number of WGCNA modules than each component alone. (C) Donut plot depicting the number of overlapping WGCNA modules between individual AT components and AT. Outside circle represents all AT-associated modules ($p < 0.05$) and is separated into the 13 modules that overlap with AT components (hashed orange) and the 3 modules unique to AT (yellow). Inner circle represents modules that are related to AT and is broken up by modules that are also unique to one AT component (FF: freezing in blue, VV: cooing in green, CC: cortisol in red) or that are shared by at least two components (shared in pink).

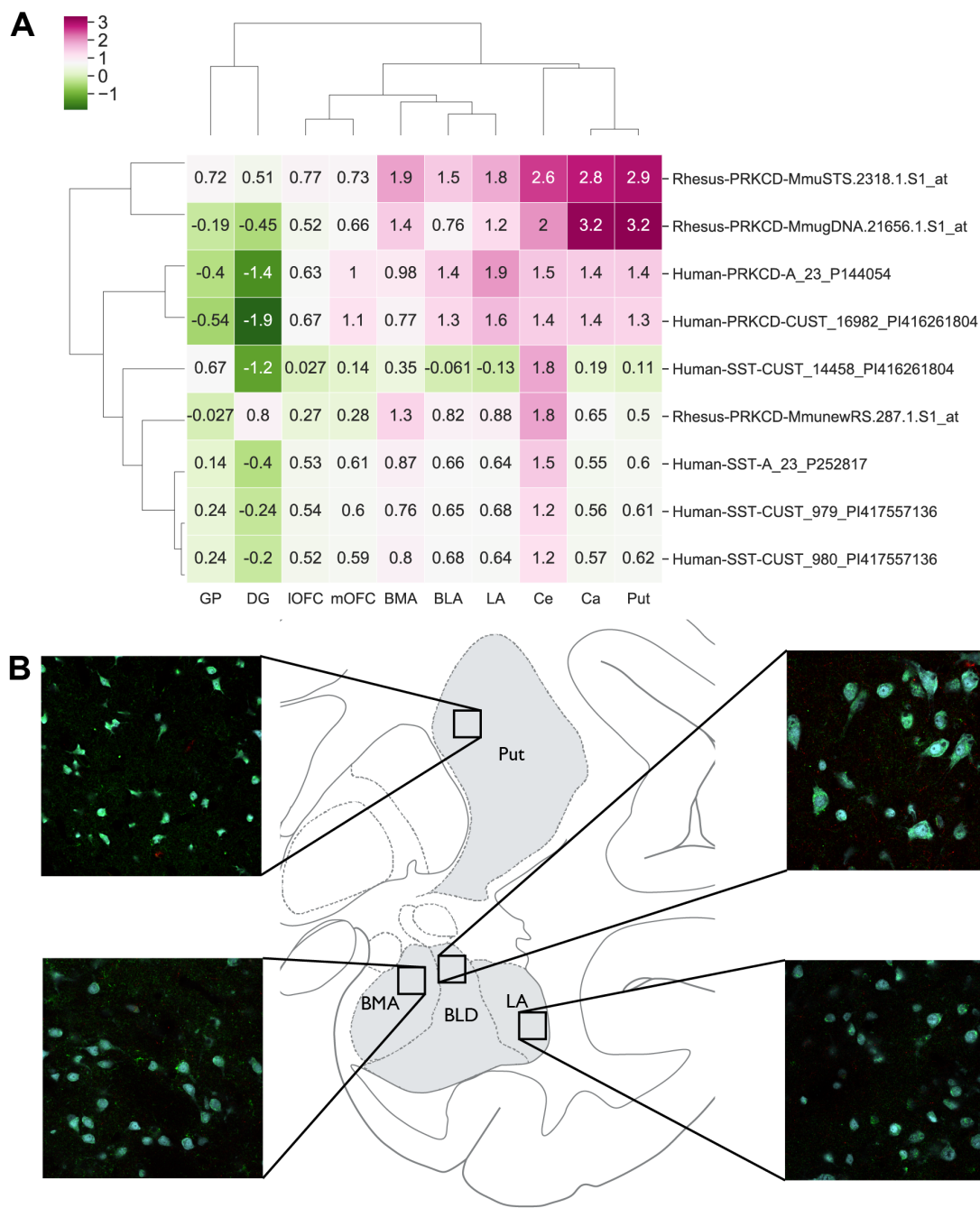


Figure S7. PRKCD mRNA and protein is widely distributed throughout the primate brain. (A) A heatmap of the human and nonhuman primate microarray data from the Allen Brain Atlas for *PRKCD* and *SST* demonstrate that the mRNA for these markers are widely distributed throughout multiple brain regions. Particular note is made of high levels of *PRKCD* in the Ce and striatum. The y-axis lists the different microarray probes for each marker for human and nonhuman primate. The x-axis describes the regions of the brain investigated. The color bar depicts the expression values, calculated using a z-score normalization of the relative expression level of each marker as compared to the rest of the brain (B). Immunofluorescence staining of PKC δ in the putamen as well as other regions of the nonhuman primate amygdala. BLD: dorsolateral division of the basal nucleus of the amygdala, BMA: basomedial nucleus of the

amygdala, LA: lateral nucleus of the amygdala, Ce: central nucleus of the amygdala, Ca = caudate, put = putamen, GP: globus pallidus, DG: dentate gyrus of the hippocampus, IOFC: lateral orbitofrontal cortex, mOFC: medial orbitofrontal cortex.

Supplemental References

1. Fox AS, Shelton SE, Oakes TR, Converse AK, Davidson RJ, Kalin NH (2010): Orbitofrontal cortex lesions alter anxiety-related activity in the primate bed nucleus of stria terminalis. *Journal of Neuroscience*. 30:7023-7027.
2. Fox AS, Shelton SE, Oakes TR, Davidson RJ, Kalin NH (2008): Trait-like brain activity during adolescence predicts anxious temperament in primates. *PLoS ONE*. 3:e2570.
3. Kalin NH, Shelton SE, Fox AS, Oakes TR, Davidson RJ (2005.): Brain regions associated with the expression and contextual regulation of anxiety in primates. *Biol Psychiatry*. 58:796-804.
4. Kalin NH, Shelton SE (1989): Defensive behaviors in infant rhesus monkeys: environmental cues and neurochemical regulation. *Science*. 243:1718-1721.
5. Granger FPBE (2007): IPython: A System for Interactive Scientific Computing. *Computing in Science & Engineering*. 9:21-29.
6. McKinney W (2010): Data Structures for Statistical Computing in Python. *Proceedings of the 9th Python in Science Conference*, pp 51-56.
7. Eric Jones TO, Pearu Peterson, others (2001): SciPy: Open source scientific tools for Python.
8. Seabold S, and Josef Perktold (2010): *Statsmodels: Econometric and statistical modeling with python*.
9. Paxinos G, Huang X, Petrides M, Toga AW (2009): *The Rhesus Monkey Brain: Stereotaxic Coordinates*. Elsevier.
10. Love MI, Huber W, Anders S (2014): Moderated estimation of fold change and dispersion for RNA-seq data with DESeq2. *Genome Biology*. 15:550.
11. Hunter JD (2007): Matplotlib: A 2D Graphics Environment. *Computing in Science & Engineering*. 9:90-95.
12. Greenfest-Allen E, Cartailler J-P, Magnuson MA, Stoeckert CJ (2017): iterativeWGCNA: iterative refinement to improve module detection from WGCNA co-expression networks. *bioRxiv*.
13. Langfelder P, Horvath S (2008): WGCNA: an R package for weighted correlation network analysis. *BMC Bioinformatics*. 9:559.
14. Klopfenstein DV, Zhang L, Pedersen BS, Ramírez F, Warwick Vesztrocy A, Naldi A, et al. (2018): GOATOOLS: A Python library for Gene Ontology analyses. *Scientific Reports*. 8:10872.
15. Kalin NH, Fox AS, Kovner R, Riedel MK, Fekete EM, Roseboom PH, et al. (2016): Overexpressing Corticotropin-Releasing Factor in the Primate Amygdala Increases Anxious Temperament and Alters Its Neural Circuit. *Biol Psychiatry*. 80:345-355.
16. deCampo DM, Fudge JL (2013): Amygdala projections to the lateral bed nucleus of the stria terminalis in the macaque: comparison with ventral striatal afferents. *J Comp Neurol*. 521:3191-3216.
17. Price JL, Russchen FT, Amaral DG (1987): The limbic region. II. The amygdaloid complex. In: Hokfelt BT, Swanson LW, editors. *Handbook of Chemical Neuroanatomy*. Amsterdam: Elsevier, pp 279-381.

18. Atlas AB (2018): Allen Brain Atlas API.: Allen Institute for Brain Science.
19. De Olmos JS (2004): The Amygdala. In: Paxinos G., Mai J.K., editors. *The Human Nervous System* 2ed. San Diego: Elsevier Academic Press.
20. Amaral DG, Price JL, Pitkänen A, Carmichael ST (1992): Anatomical organization of the primate amygdaloid complex. *The Amygdala: Neurobiological Aspects of Emotion, Memory, and Mental Dysfunction*: Wiley-Liss, Inc., pp 1-66.
21. Gundersen HJ (1986): Stereology of arbitrary particles. A review of unbiased number and size estimators and the presentation of some new ones, in memory of William R. Thompson. *Journal of microscopy*. 143:3-45.
22. West MJ, Slomianka L, Gundersen HJ (1991): Unbiased stereological estimation of the total number of neurons in the subdivisions of the rat hippocampus using the optical fractionator. *The Anatomical record*. 231:482-497.
23. Oler JA, Tromp DP, Fox AS, Kovner R, Davidson RJ, Alexander AL, et al. (2017): Connectivity between the central nucleus of the amygdala and the bed nucleus of the stria terminalis in the non-human primate: neuronal tract tracing and developmental neuroimaging studies. *Brain Struct Funct*. 222:21-39.
24. Rosene DL, Roy NJ, Davis BJ (1986): A cryoprotection method that facilitates cutting frozen sections of whole monkey brains for histological and histochemical processing without freezing artifact. *J Histochem Cytochem*. 34:1301-1315.
25. Fox AS, Oler JA, Shackman AJ, Shelton SE, Raveendran M, McKay DR, et al. (2015): Intergenerational neural mediators of early-life anxious temperament. *Proc Natl Acad Sci U S A*. 112:9118-9122.
26. Oler JA, Fox AS, Shelton SE, Rogers J, Dyer TD, Davidson RJ, et al. (2010): Amygdalar and hippocampal substrates of anxious temperament differ in their heritability. *Nature*. 466:864-868.
27. Shackman AJ, Fox AS, Oler JA, Shelton SE, Davidson RJ, Kalin NH (2013): Neural mechanisms underlying heterogeneity in the presentation of anxious temperament. *Proc Natl Acad Sci U S A*. 110:6145-6150.
28. Kalin NH, Shelton SE, Davidson RJ (2004): The role of the central nucleus of the amygdala in mediating fear and anxiety in the primate. *J Neurosci*. 24:5506-5515.
29. Oler JA, Fox, A.S., Shackman, A.J., and Kalin, N.H. (2016): The central nucleus of the amygdala is a critical substrate for individual differences in anxiety. In Living without an Amygdala. *In Living without an Amygdala*. New York, NY: Guilford Press, pp 218-251.
30. Zimin AV, Cornish AS, Maudhoo MD, Gibbs RM, Zhang X, Pandey S, et al. (2014): A new rhesus macaque assembly and annotation for next-generation sequencing analyses. *Biology Direct*. 9:20.